

# **Vibration-Induced Crack Tip Flipping: A Closer Look at an Unfamiliar Phenomenon in Pipeline Failure Analysis**

Benoît Paermentier<sup>a</sup>, Steven Cooreman<sup>b</sup>, Sam Coppieters<sup>a</sup>, Reza Talemi<sup>a</sup>

<sup>a</sup>Elooi Laboratory, Department of Materials Engineering, KU Leuven, Ghent Campus, Belgium

<sup>b</sup>ArcelorMittal Global R&D Gent/OCAS N.V., Zelzate, Belgium

[benoit.paermentier@kuleuven.be](mailto:benoit.paermentier@kuleuven.be)

## **Abstract**

Fracture propagation control is an essential strategy to avoid a catastrophic event involving both economic losses and environmental damage. The Dynamic Tensile Tear Test (DT3) was introduced as an alternative tool to characterise dynamic fracture behaviour of high-strength pipeline steels. Mimicking the in-service loading conditions by imposing a dynamic tensile load, the obtained fracture surfaces closely resemble those observed in full-scale pipeline burst tests. A phenomenon called Crack Tip Flipping (CTF) could also be observed in combination with the formation of Arrowhead Markings (AHMs). The mechanisms provoking these phenomena and their effect on the fracture resistance of the pipeline material have not yet been investigated with respect to pipeline failure. Therefore, a high-speed stereo DIC setup was used to study the fracture behaviour of X70 grade pipeline steel. The DIC setup identified a mechanical out-of-plane vibration that resulted in an additional torsional loading component. Numerical models were constructed with implementation of the Modified Bai-Wierzbicki (MBW) damage model to validate the experimental observations. Imposing a vibration-induced out-of-plane component resulted in a nearly identical fracture behaviour as observed during experiments. Both the crack path and the final fracture surface could be reproduced. Based on the obtained data, it is suggested that this oscillation causes a rotation of the stress tensor controlled by the through-thickness shear component. As a result, the stress state at the crack front is oriented towards the plane of maximum shear, forming a slanted fracture surface. Notably, the additional torsion load did not affect the load-displacement curve, as the value of the effective stress remains unaffected. Consequently, the fracture resistance, computed from energy values extracted from the load-displacement curve, are not influenced by the occurrence of CTF or the formation of AHMs. Conversely, based on the discussed mechanism of CTF, its presence could indicate the conditions under which pipeline failure occurred.

Keywords: Dynamic Tensile Tear Test; Dynamic Crack Propagation; Crack Tip Flipping; Digital Image Correlation; FEM; Modified Bai-Wierzbicki

## Nomenclature

### Acronyms

AHM	Arrowhead Marking
BW	Bai-Wierzbicki
CCS	Carbon Capture and Storage
CDM	Continuum Damage Model
CMOD	Crack Mouth Opening Displacement
CTF	Crack Tip Flipping
CTOA	Crack Tip Opening Angle
CVN	Charpy V-Notch
DIC	Digital Image Correlation
DIL	Damage Initiation Locus
DT3	Dynamic Tensile Tear Test
DWTT	Drop Weight Tear Test
EDM	Electric Discharge Machining
FE	Finite Element
FEA	Finite Element Analysis
FOV	Field Of View
LVDT	Linear Variable Differential Transformer
MBW	Modified Bai-Wierzbicki
SEM	Scanning Electron Microscope

### Symbols

$a$	Crack length
$c_1, c_2, c_3, c_4$	Material dependent DIL constants
$c_1^T, c_2^T, c_3^T$	Temperature correction factors
$c_1^{\dot{\epsilon}}, c_2^{\dot{\epsilon}}, c_3^{\dot{\epsilon}}$	Strain rate correction factors
$c_1^{crit}, c_2^{crit}$	Critical damage parameters
$c_\eta, c_\theta^s, c_\theta^l, c_\theta^c, m$	Stress state parameters
$n$	Strain hardening exponent
$B_0$	Initial thickness
$D$	Damage variable
$D_{crit}$	Critical damage variable
$E$	Young's modulus
$E_f$	Characteristic dissipation energy
$I_1, J_2, J_3$	Invariants of the stress tensor
$K$	Strength coefficient
$S_x$	Normal stress component along x-axis
$S_z$	Normal stress component along z-axis

$S_{xz}$	Shear stress component along xz-plane
$T$	Temperature
$\bar{\varepsilon}_p$	Equivalent plastic strain
$\bar{\varepsilon}_i$	Damage initiation strain
$\dot{\bar{\varepsilon}}_p$	Equivalent plastic strain rate
$\eta$	Stress triaxiality
$\theta$	Lode angle
$\bar{\theta}$	Normalised Lode angle parameter
$\theta_p$	Angle of maximum principal stress
$\sigma_1, \sigma_2, \sigma_3$	Principal stresses
$\sigma_m$	Mean stress
$\sigma_y$	Yield stress
$\bar{\sigma}$	von Mises equivalent stress
$\bar{\sigma}(\bar{\varepsilon}^{pl})$	Flow curve
$\Phi$	Flow potential

## 1 Introduction

A network of high-pressure pipelines still is the most efficient means of transport for gas products such as natural gas, carbon dioxide, hydrogen, etc. [1]. Safe pipeline design and operation heavily relies on data obtained from lab-scale experiments making them an essential tool to qualify materials for pipeline applications. Consequently, materials must fulfil minimum toughness requirements to ensure structural integrity over several decades. With the development of modern high-strength steel grades, it has become clear that traditional impact testing is not representative for pipeline failures [2, 3, 4]. Moreover, aforementioned testing techniques have been shown to result in non-conservative predictions. Therefore, characterisation of pipeline steels and requirements for pipeline applications should transition to material experimentation representative of in-service conditions. The Dynamic Tensile Tear Test (DT3) has been investigated with the aim to provide a lab-scale alternative for material characterisation of pipeline steels through impact testing. The DT3 was introduced by Rivalin et al. [5, 6] and has been successfully used in several investigations [7, 8]. Most recent work [8] focussed on the characterisation of the dynamic fracture behaviour using the experimental setup. This was achieved through data such as resistance curve (energy-based), Crack Tip Opening Angle (CTOA), and Crack Mouth Opening Displacement (CMOD) obtained using high-speed imaging. Moreover, based on 3D scans and microscopic SEM analysis, it could be

concluded that the obtained ductile fracture surfaces are closely related to the fracture surface of full-scale burst tests. The fracture morphology is a crucial aspect in identifying the cause of failure as the failure conditions are reflected in the type of fracture surface. In general, the ductile fracture morphology of burst-tested high-grade pipeline steel is characterised by ductile slant with brittle splitting features at centre-thickness [9]. In contrast, the CVN fracture surface provides limited correlation to ductile slant. The DWTT fracture surface can show ductile slant but only over a relatively small section. Furthermore, a study by Santos Pereira et al. [10] showed that only 17% of the total absorbed energy during the DWTT tests is associated to stable crack propagation. Consequently, both CVN and DWTT methods present limitations in energy-based characterisation of crack propagation resistance of modern pipeline steels. The DT3 specimen provides a long fracture ligament with the same characteristics as observed on burst tested material, a long ductile slant ligament including splitting along the centreline. Notably, in latest work [8], it was reported that the ductile slant alternated between shear planes. This phenomenon could also be observed – using high-speed cameras – as “zig-zag” crack progression on the specimen surface. This type of crack progression results in a typical shark tooth-like pattern on the specimen surface. The same behaviour was reported by Chattopadhyay et al. [11] when performing burst tests on large diameter pipes

Only a limited number of studies have been performed regarding this topic. Simonsen and Törnqvist [12] observed the alternating slant behaviour during quasi-static testing on large steel plates. In contrast, Rivalin et al. [5] performed the DT3 experiment on steel plates under both quasi-static and dynamic conditions. The quasi-static fracture surfaces appeared uniform whilst an alternating slant fracture surface was obtained solely under dynamic conditions. Combining the alternating slant observations of Simonsen and Törnqvist (quasi-static conditions) and Rivalin et al. (dynamic conditions) suggests that the phenomenon is not necessarily dependent on loading rate. Felter et al. [13] observed the alternating behaviour on quasi-static tensile tests on aluminium sheets and referred to this phenomenon as assisted crack-tip flipping (CTF). It was suggested that imposing a slight out-of-plane movement or torsion type loading could provoke the CTF mechanism. It should be noted that, most studies provoke the CTF phenomenon by imposing an additional loading component during quasi-static testing. In contrast, the CTF occurrence in the DT3 experiment is not deliberately provoked. Based on a numerical study, Nielsen and Felter [14] later concluded that the CTF phenomenon only occurs within a limited range of material parameters. Subsequently, Nielsen and Gundlach [15] used

X-ray tomography to conclude that the slanted fracture face flip is caused by growing shear-lips near the outer surface behind the leading slanted tip.

Even though the mechanism of the CTF phenomenon is being debated, the effects on experimental data used for predictive tools have not yet been discussed. Furthermore, its presence on pipeline fracture surfaces and its relevance for pipeline failure analysis have not yet been investigated. Currently, CTF is mainly regarded as – and investigated as – an experimental artefact. Notably, the phenomenon is primarily observed on experiments aiming to mimic loading conditions of in-service pipelines, such as the MDCB and DT3 setup. However, no pipeline failure report has indicated the presence of CTF on the pipe fracture surface. Still, in some cases, images showing the CTF phenomenon on circumferential and longitudinal cracked pipes can be found in both in-field failures as well as burst tested pipes (as shown in Figure 1). In both the field reports and the post-test analysis, the presence of the CTF on the fracture surface is not specified nor is it described. Consequently, the question is raised whether CTF is a phenomenon to consider in pipeline failure analysis.

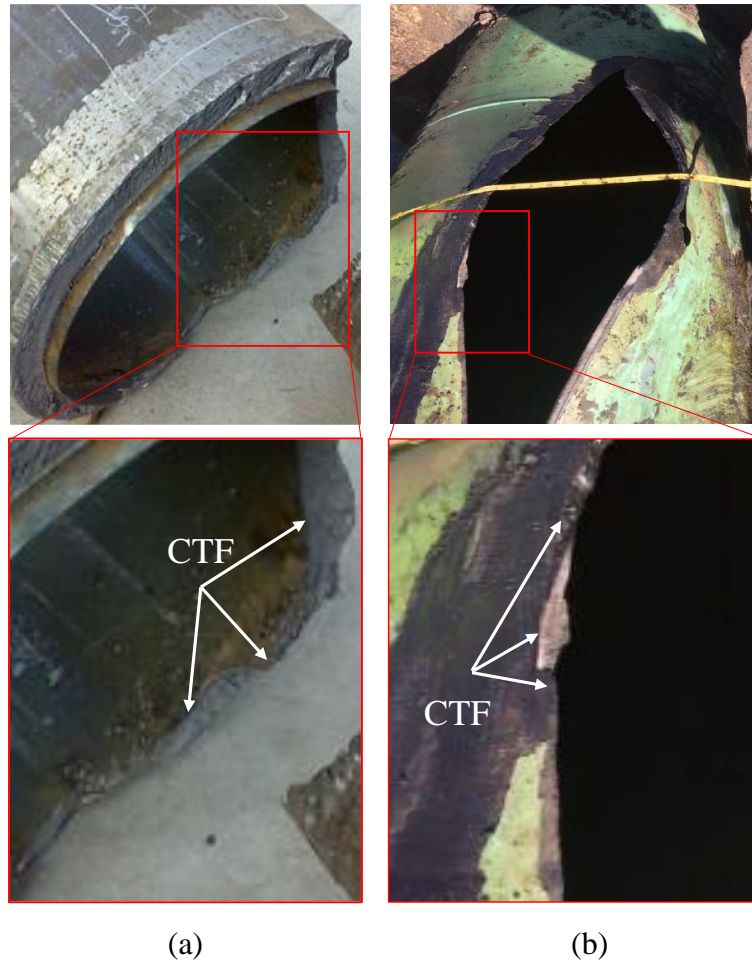


Figure 1: CTF phenomenon along the circumference of a hydrogen induced failure of an X60 grade pipeline [16] (a) and along a longitudinal in-field failure of an X70 grade pipeline [17] (b).

Furthermore, the database of full-scale burst tests on high-grade steel are still limited and in case of field reports, the metallurgic analysis is often redacted. If CTF is a result of an out-of-plane movement – or torsion type loading – it could provide essential insight into the loading conditions at the time of failure. Moreover, it is not unlikely that external parameters can introduce an out-of-plane oscillation to in-field conditions. Actually, accidental damage due to excavations is considered a leading cause of pipeline failure incidents [18].

To assess the CTF mechanism, its relevance for pipeline failure analysis, and its effect on measured data, an optical full-field measurement technique called Digital Image Correlation (DIC) is used in this study. DIC is often used in material characterisation and reverse identification procedures. However, these procedures mainly consider quasi-static experimentation with a low loading rate. As this study aims to identify the dynamic fracture behaviour at high loading rates, additional challenges arise. It should be considered that a high frame rate is required to capture enough images. However, increasing the frame rate limits the

achievable image resolution, which is essential for the image correlation procedure. In recent work [8], the resolution of obtained images (384 x 256) was not satisfactory for the implementation of DIC. Consequently, for this series of tests, a compromise between image resolution and frame rate was made in order to capture enough images whilst still providing an acceptable correlation coefficient. In comparison to previous work, the image resolution was increased ( $1280 \times 720$ ) and the frame rate was reduced (5700 fps). To validate the obtained experimental results, a Finite Element Analysis (FEA) was performed. Plastic material behaviour, damage and failure were considered through the integration of the Modified Bai-Wierzbicki (MBW) damage model. Using the DT3 experiment in combination with high-speed stereo DIC and finite element models provides a better insight into the dynamic fracture behaviour of high-grade pipeline steel.

In the following section, a description of the experimental DT3 setup including equipment and instrumentation is provided. Subsequently, the numerical simulations and material models are discussed. Finally, experimental and numerical data are assessed and elaborated followed by the formulation of general conclusions.

## 2 Experimental Setup

### 2.1 General

The experimental DT3 setup is a destructive lab-scale test that uses a dynamic tensile load to fracture a full-thickness specimen. A schematic overview of the DT3 setup and the testing procedure is shown in Figure 2. The setup utilises four hydraulic cylinders to reach a maximum tensile load of 4000 kN. During the load build-up, resulting from the cylinder extension, a set of heavy disc springs is compressed. Once a crack initiates in the specimen, the stored elastic energy is released and dynamic fracture is achieved. Consequently, the testing procedure can be characterised by two phases: a quasi-static phase (cylinder extension) and a dynamic phase (spring energy release). The high tensile force in combination with the dynamic nature of the fracture phase results in high reaction forces acting on the system. Therefore, the system is constructed on two rail-driven frames; one frame carries the four hydraulic cylinders whilst the second frame carries the set of disc springs. Once the dynamic fracture occurs, the two frames move away from each other, dissipating all remaining energy. Shock absorbers on each side of the rail ensure all excess energy is diffused and prevents damage to the system.

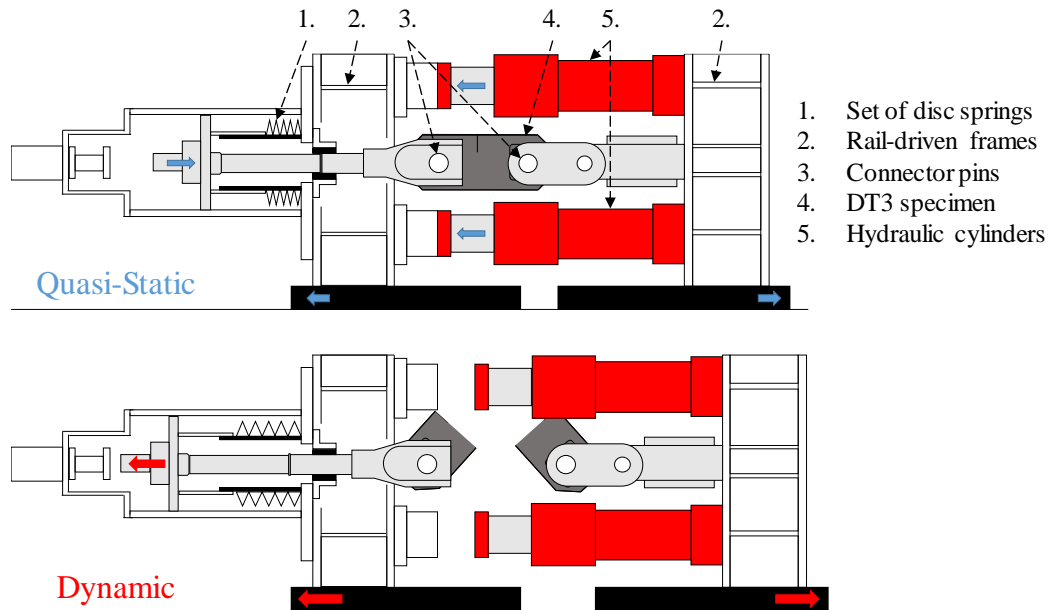


Figure 2: Schematic representation of the DT3 testing equipment with quasi-static phase (top), and dynamic phase (bottom).

The specimen geometry is designed with pipeline rupture in mind as it mimics the loading conditions of a longitudinal crack propagating in an in-service pipeline. In this study, test samples were constructed from X70 grade pipeline steel with a thickness of 14.2 mm. An initial notch of 78 mm was created using a wire Electric Discharge Machining (EDM) procedure. Consequently, a total fracture ligament of 172 mm is obtained. It should be noted that the DT3 sample is a flat plate and is not bent. The specimen is flattened from coil material into a plate-like geometry using roll levelling to minimise residual stresses. For a more detailed description of specimen production, the reader is referred to [8].

## 2.2 Instrumentation

Experimental load and displacement data were obtained using a high-speed LVDT positioned between the two connector pins and a load cell along the loading axis, respectively. All data was logged at a frequency of 500 kHz using a high-speed Dewetron Trendcorder system. Two Phantom VEO640L high-speed cameras were used to capture crack propagation at a frame rate of 5700 fps over a total time period of 10 seconds. The Trendcorder system allowed triggering of the camera setup based on real-time displacement data. During this series of experiments, a displacement of 10 mm was selected as trigger point. At this displacement value, it can be assumed with certainty that fracture initiation has occurred. Consequently, an image capture distribution of 9s pre-trigger and 0.5s post-trigger was selected. The camera positioning in combination with a resolution of  $1280 \times 720$  pixels resulted in a Field of View (FOV) of 268.8

× 151.2 mm. Two high-intensity LED lights were required to obtain uniform exposure due to the ambient lighting conditions and high frame rate. Figure 3 provides an overview of the experimental setup and the resulting FOV.

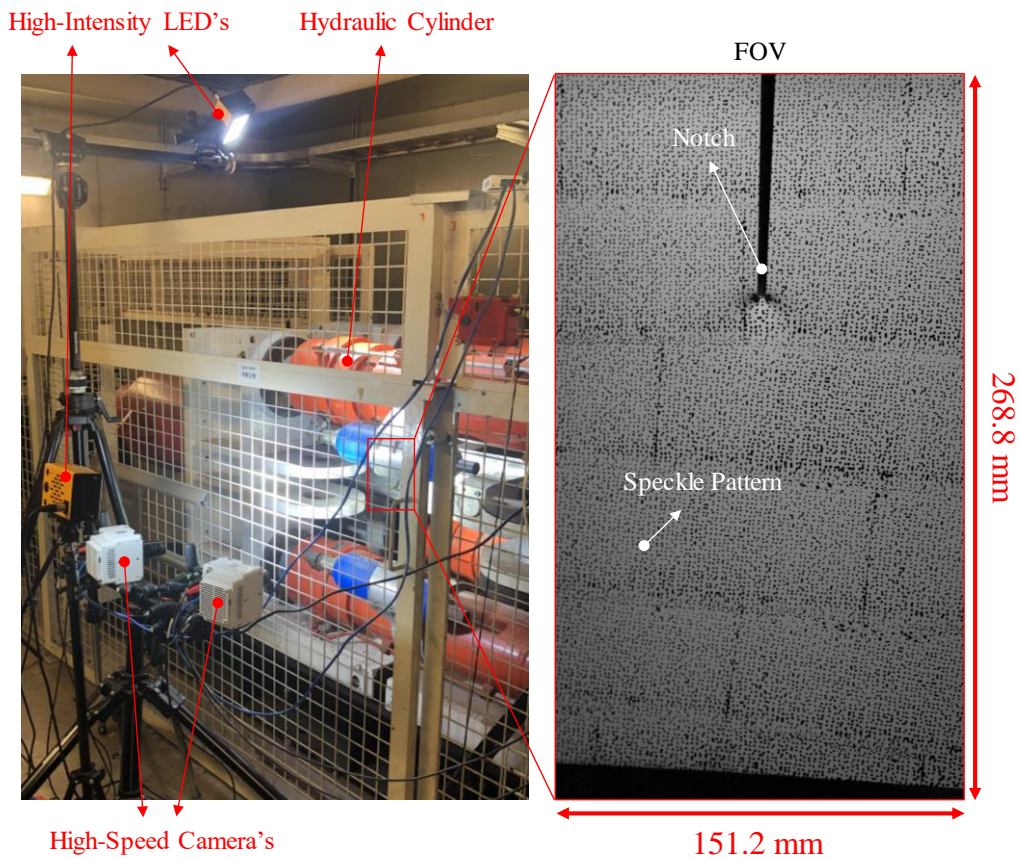


Figure 3: Overview of the experimental testing setup (left), and resulting camera FOV (right).

Sample preparation consisted of sandblasting and degreasing before applying a speckle pattern to the specimen surface. Subsequently, a white base coating is painted on the sample surface, and the speckle pattern is applied using a MatchID speckle kit. A consistent speckle size of 1 mm guaranteed a good quality of the subsequent image correlation. Both calibration and stereo image correlation was performed using MatchID software [19]. Calibration of the camera setup was performed before actual fracture testing verifying the accuracy of the setup.

In the following, the four tests are respectively referred to as test 1 to test 4. All experiments were performed at room temperature. High-speed images were successfully captured for each of the four tests. Furthermore, the stereo DIC procedure was successfully applied to each test. Obtained images and DIC data are discussed in the results section.

## 2.3 Material Properties

The DT3 specimens were constructed out of API X70 grade steel. The chemical composition of this ferritic-pearlitic steel was determined using a spark emission spectrometer and reported in previous work [8, 20]. Mechanical properties were obtained from quasi-static tensile tests [21]. The work hardening is modelled and implemented in the FE model using Ludwik's law, which reads as:

$$\bar{\sigma}(\bar{\varepsilon}_p) = \sigma_y + K(\bar{\varepsilon}_p)^n$$

With  $K$  defined as the strength coefficient, and  $n$  is defined as the strain hardening exponent. Table 1 provides an overview of the tensile properties for the considered X70 material.

Table 1: Mechanical material properties for X70 grade pipeline steel.

$E$ [GPa]	$\sigma_y$ [MPa]	$K$ [MPa]	$n$ [-]
210	520	473	0.3023

## 3 Numerical Modelling

### 3.1 General

Finite element (FE) models were created to validate the results obtained from the experimental setup including the high-speed DIC procedure. Numerical models were created in the commercial FE software ABAQUS [22] which provided the opportunity to investigate the CTF mechanics in more depth than possible with the available experimental data. Damage and failure were considered using the Modified Bai-Wierzbicki (MBW) damage model. Implementation of the MBW model was achieved using a user-defined VUMAT subroutine. This material model was selected since it considers the effects of loading rate and stress state on the mechanism of damage and failure. Previous work has also shown the model is capable of providing a good correlation with experimental data in case of the DT3 experiment.

### 3.2 Modified Bai-Wierzbicki (MBW)

In this study, material behaviour is considered through the implementation of the Modified Bai-Wierzbicki model (MBW) as described by Lian et al [23]. This model implements both plasticity and damage characteristics. The former follows the uncoupled plasticity model as described by Bai and Wierzbicki [24] whilst the latter is taken into account using a local Continuum Damage Mechanics (CDM) based damage evolution law, which allows material

degradation. Stress state dependence of plastic deformation is considered using the stress triaxiality and Lode angle parameter, which are referred to as  $\eta$  and  $\bar{\theta}$ , respectively. In order to define aforementioned parameters, the stress state of an isotropic material is described as a function of the principal stresses ( $\sigma_1$ ,  $\sigma_2$  and  $\sigma_3$ ) and the invariants of the Cauchy stress tensor  $\boldsymbol{\sigma}$  with its deviatoric part  $\mathbf{s}$ . Consequently, stress triaxiality  $\eta$  and Lode angle  $\theta$  can be written accordingly:

$$\eta = \frac{\sigma_m}{\bar{\sigma}} = \frac{I_1}{3\sqrt{3}J_2} = \frac{(\sigma_1 + \sigma_2 + \sigma_3)}{3\sqrt{\frac{1}{2}[(\sigma_1 - \sigma_2)^2 + (\sigma_2 - \sigma_3)^2 + (\sigma_3 - \sigma_1)^2]}} \quad (1)$$

$$\theta = \frac{1}{3} \cos^{-1} \left( \frac{3\sqrt{3}}{2} \frac{J_3}{J_2^{3/2}} \right) \quad (2)$$

with  $\sigma_m$  defined as the mean stress, and  $\bar{\sigma}$  defined as the von Mises equivalent stress. Normalising the Lode angle results in the Lode angle parameter  $\bar{\theta}$ , which has a value range of  $-1 \leq \bar{\theta} \leq 1$ . This conversion is shown in following equation:

$$\bar{\theta} = 1 - \frac{6\theta}{\pi} = 1 - \frac{2}{\pi} \cos^{-1} \left( \frac{3\sqrt{3}}{2} \frac{J_3}{J_2^{3/2}} \right) \quad (3)$$

Consequently, the yield function with consideration of stress state, temperature, and strain rate effects can be expressed as:

$$\begin{aligned} \Phi = \bar{\sigma} & - \underbrace{\left[ \bar{\sigma}(\bar{\varepsilon}_p) \left( c_1^{\dot{\varepsilon}} \cdot \ln \dot{\varepsilon}_p + c_2^{\dot{\varepsilon}} \cdot \dot{\varepsilon}_p \right) + c_3^{\dot{\varepsilon}} \cdot \dot{\varepsilon}_p \right]}_{f(\bar{\varepsilon}_p, \dot{\varepsilon}_p)} \times \underbrace{\left[ c_1^T \cdot \exp(-c_2^T \cdot T) + c_3^T \right]}_{f(T)} \\ & \times \underbrace{\left[ 1 - c_\eta (\eta - \eta_0) \right]}_{f(\eta, \bar{\theta})} \times \underbrace{\left[ c_\theta^s + (c_\theta^{ax} - c_\theta^s) \left( \lambda - \frac{\lambda^{m+1}}{m+1} \right) \right]}_{f(\eta, \bar{\theta})} (1 - D) \leq 0 \end{aligned} \quad (4)$$

with

$$\lambda = \frac{\cos\left(\frac{\pi}{6}\right)}{1 - \cos\left(\frac{\pi}{6}\right)} \left( \frac{1}{\cos\left(\theta - \frac{\pi}{6}\right)} - 1 \right) \quad (5)$$

$$c_{\theta}^{ax} = \begin{cases} c_{\theta}^t & \text{if } \bar{\theta} \geq 0 \\ c_{\theta}^c & \text{if } \bar{\theta} < 0 \end{cases} \quad (6)$$

where  $f(\bar{\varepsilon}_p, \dot{\bar{\varepsilon}}_p)$ ,  $f(T)$  and  $f(\eta, \bar{\theta})$  are functions to account for the effects of strain rate, temperature, and stress state, respectively. Material dependent parameters include  $c_1^{\dot{\varepsilon}}$ ,  $c_2^{\dot{\varepsilon}}$  and  $c_3^{\dot{\varepsilon}}$  for strain rate dependence,  $c_1^T$ ,  $c_2^T$  and  $c_3^T$  for temperature dependence, constants  $c_{\eta}$ ,  $c_{\theta}^s$ ,  $c_{\theta}^t$ ,  $c_{\theta}^c$  and  $m$  are stress state parameters. Consequently, the stress state dependence is taken into account as the flow potential is written as a function of the defined stress state parameters. Internal parameter  $D$  is a scalar representing the accumulated damage, which induces softening and thus affects the yield potential.

The coupled damage evolution law considers the physical mechanisms of ductile failure: void nucleation, growth and coalescence. The effect of damage on the flow function is neglected until a critical amount of equivalent plastic strain  $\bar{\varepsilon}_i$  is reached. It is assumed that this critical strain value is required to initiate void nucleation, or in other words, is required for damage to occur. The damage initiation strain is defined with respect to the Lode angle parameter  $\bar{\theta}$  :

$$\bar{\varepsilon}_i = (c_1 e^{-c_2 \eta} - c_3 e^{-c_4 \eta}) \bar{\theta}^2 + c_3 e^{-c_4 \eta} \quad (7)$$

$c_1$  to  $c_4$  are material constants determined through experimental calibration. Consequently, strain value  $\bar{\varepsilon}_i$  indicates the point where the material behaviour cannot be described using the plasticity model and the damage softening needs to be accounted for. This implies that damage parameter  $D$  remains zero until critical strain value  $\bar{\varepsilon}_i$  is reached. The damage evolution law defining parameter  $D$ , assumes that a characteristic amount of energy  $E_f$  is dissipated throughout the damage process. Representing the accumulated damage, parameter  $D$  is defined as:

$$D = \frac{\sigma_{y0}}{E_f} \int_{\bar{\varepsilon}_i}^{\bar{\varepsilon}} d\bar{\varepsilon}_p \quad (8)$$

$\sigma_{y0}$  is defined as the yield stress at the onset of damage and  $E_f$  is the fracture dissipation energy. As damage progresses, parameter  $D$  increases in value, representing void growth until

void coalescence is reached. Void coalescence or material failure is considered once critical value  $D_{crit}$  is reached:

$$D_{crit} = c_1^{crit} \bar{\theta}^2 + c_2^{crit} \quad (9)$$

The damage evolution law can be described in terms of internal parameter  $D$  with respect to the evolution of the equivalent plastic strain  $\bar{\varepsilon}_p$ :

$$D = \begin{cases} 0 & \text{if } \bar{\varepsilon}_p \leq \bar{\varepsilon}_i \\ \frac{\sigma_{y0}}{E_f} \int_{\bar{\varepsilon}_i}^{\bar{\varepsilon}} d\bar{\varepsilon}_p & \text{if } \bar{\varepsilon}_i < \bar{\varepsilon}_p < \bar{\varepsilon}_f \\ D_{crit} & \text{if } \bar{\varepsilon}_p = \bar{\varepsilon}_f \end{cases} \quad (10)$$

with  $\bar{\varepsilon}_f$  referred to as the strain at which final failure occurs. More information on the governing equation can be found in the studies by Lian et al. [23], Novoksharov et al. [21], and Wu et al. [25]. A summary of the MBW parameters used in this study are available in literature [21] and are reported in previous work [8].

### 3.3 Loading and Boundary Conditions

A total of two 3D Finite Element (FE) models were constructed, one reference model which has been successfully applied in a previous study [8], and one CTF model which considers an additional out-of-plane deformation based on the measured DIC data. Other than the loading condition, the two models have an identical meshing strategy, material definition as well as identical boundary conditions. The geometry and meshing strategy of the models is shown in Figure 4.

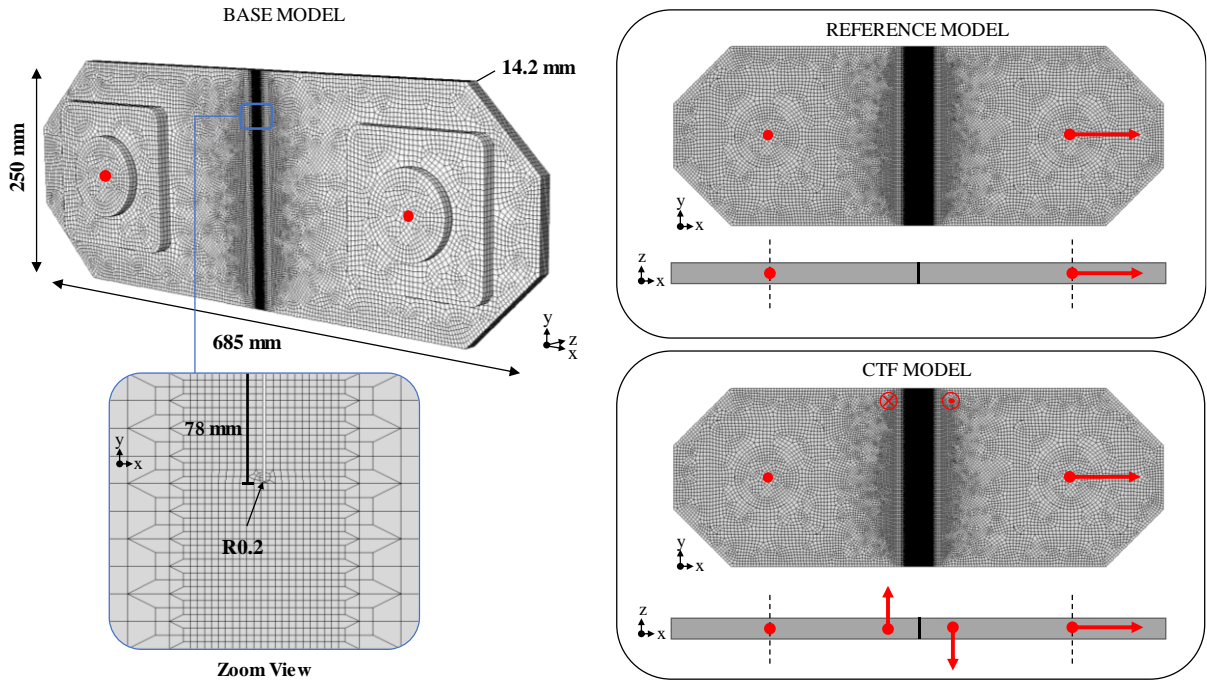


Figure 4: An overview of the geometry and meshing strategy of the base model (left) and different loading conditions for the reference model and the CTF model (right).

In the fracture region, the element size measured  $0.5 \times 0.5 \times 0.5$  mm. A uniform element distribution was achieved using a structured partitioning strategy obtained through an in-house Python script. Boundary conditions were applied to the connector pins except for the out-of-plane displacement. One pin serves as a fixed point and is constrained in all translation directions whilst the second pin is allowed to translate along the loading axis. Similar to the experimental test procedure, the numerical model consists of two phases. During the first step, a quasi-static pin velocity is applied to the second pin mimicking the cylinder extension. The second step applies a dynamic velocity gradient based on the measured pin velocity during the DT3 experiment. The experimental system stiffness was calculated to be 275 kN/mm by applying a linearly increasing load. This stiffness is used to compensate the material response obtained from the numerical model. Consequently, the stiffness of the FE model is reduced to mimic the measured stiffness of the experimental setup.

As mentioned above, the CTF model considers an additional torsional loading component. During the dynamic step, an out-of-plane oscillating displacement is applied to the top part of the specimen as shown in Figure 5 (a) and Figure 5 (b).

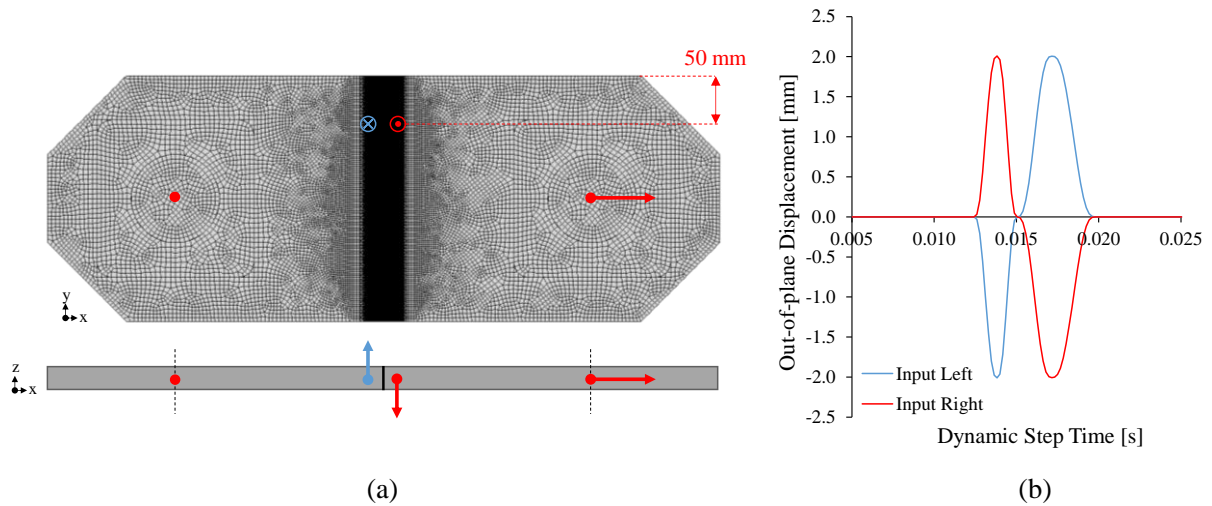


Figure 5: Overview of the loading conditions of the CTF model (a), input used to model the out-of-plane displacement during the dynamic step (b).

This torsional loading input is based on the out-of-plane displacement obtained from the stereo DIC procedure. Data extraction was performed on the location shown in Figure 5 (a). This data indicates a phase shift of  $180^\circ$  between the left out-of-plane displacement and right out-of-plane displacement. The experimental vibration frequency is identical to the input of the numerical model. However, the amplitude is increased to ensure the consideration of the worst-case scenario.

## 4 Results and Discussion

### 4.1 Experimental Results

#### 4.1.1 DT3 Data Analysis

The obtained load-displacement data, plotted in Figure 6, is consistent with the data obtained from previous investigations [8]. However, the measured peak load of 1140 kN is approximately 5% higher than the 1080 kN measured during previous experiments. This deviation could be caused by the implementation of a different logger system, which required recalibration.

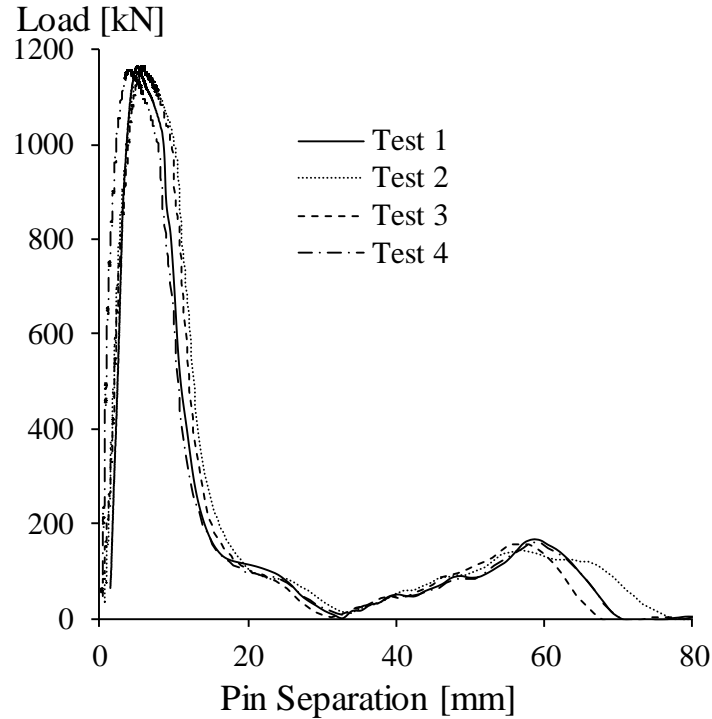


Figure 6: Experimental load-displacement data.

Synchronisation of the images together with the load-displacement data reveals the three phases of dynamic failure: crack growth, dynamic crack propagation, and final tear-off. It can be observed in Figure 7 that the crack extension during the initial phase is limited. A crack length of 12 – 15 mm is visible on the surface, which is in the same order of magnitude as the nominal thickness of the specimen. After reaching the peak load, approximately 4 seconds of quasi-static crack growth is observed before the transition into a dynamic propagating crack occurs. In contrast, the dynamic crack progression is characterised by significant crack extension over a time period in the order of milliseconds – up to 8 ms. The final tear-off phase can be considered a combination of previous phases in the sense that it occurs within milliseconds but only shows a limited amount of crack extension. These observations suggest that the relevant load-displacement data for the characterisation of dynamic fracture behaviour is mainly situated in the failure second phase.

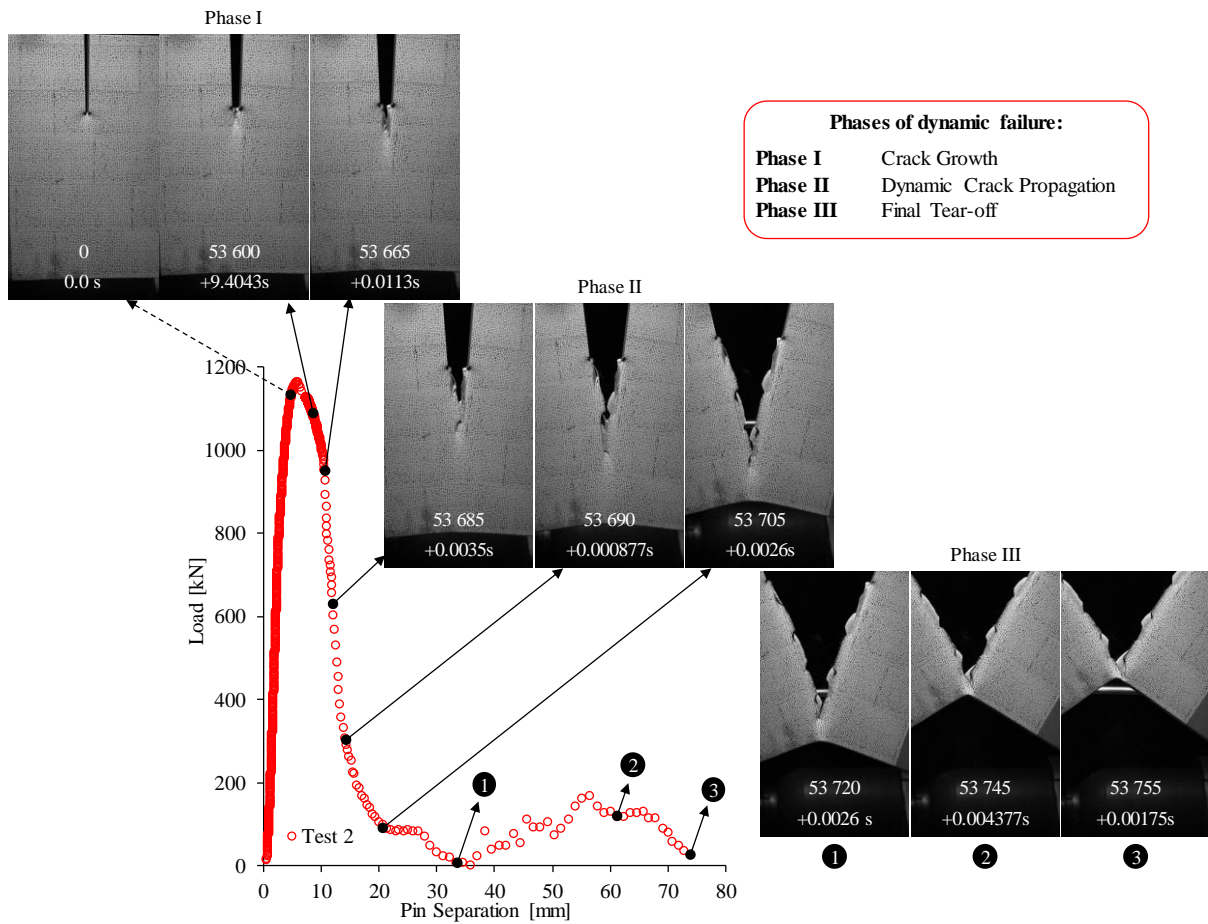


Figure 7: Synchronised images captured during the DT3 test procedure and the indication of three phases of dynamic failure.

Furthermore, Figure 7 indicates that the phenomenon of CTF exclusively occurs in the dynamic crack propagation phase. Fractography of the resulting fracture surfaces confirms this observation. Figure 8 (a) shows a 3D scan of the fractured specimen obtained from test 2. Based on the section views, the crack growth phase can be characterised by flat fracture before transitioning into a single slant fracture appearance typical for the dynamic propagation phase. During this dynamic phase, the CTF phenomenon can be identified by the frequent tilting or “flipping” of the slant direction. Figure 8 (b) provides a better view on the region where a flip occurs.

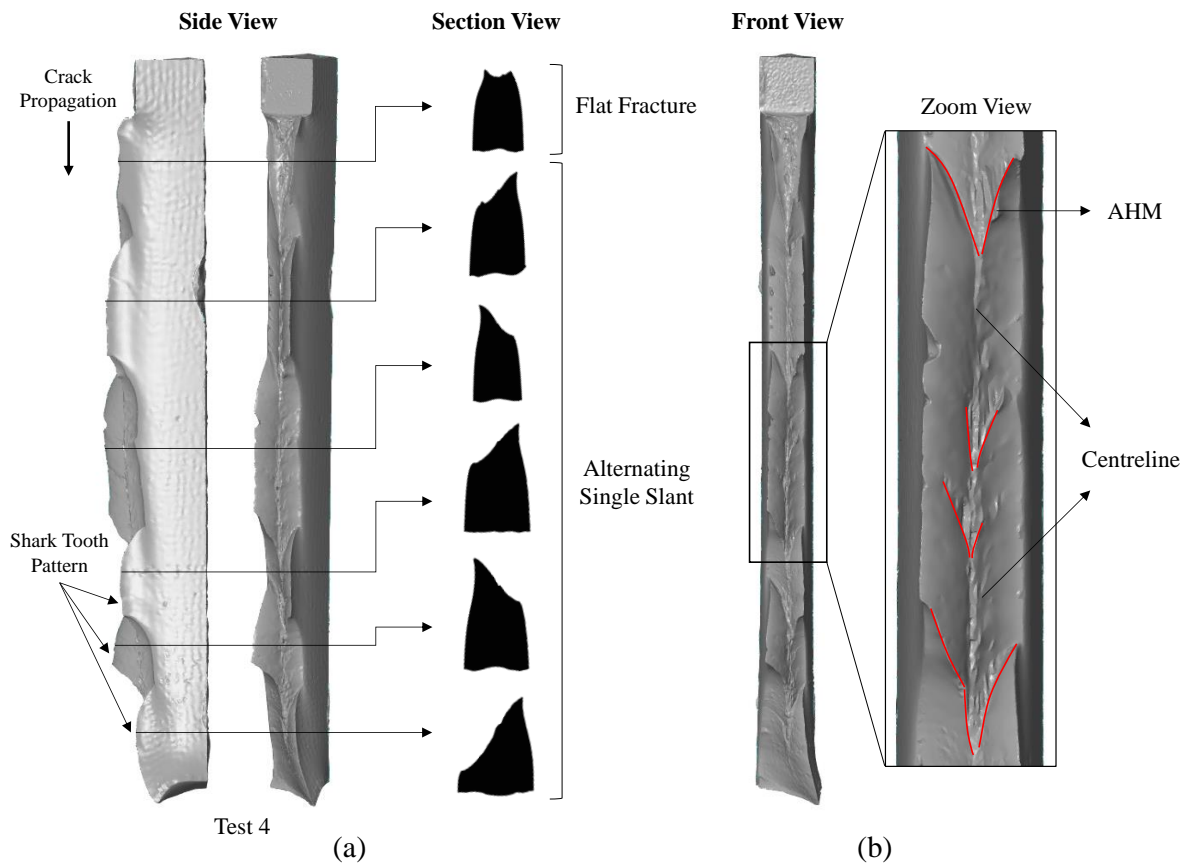


Figure 8: Scanned 3D specimen with section view indicating alternating ductile slant behaviour (a) and 3D scan showing the characteristic AHM along the centreline between subsequent slant transitions (b).

Throughout the propagation regions, a distinct arrowhead marking (AHM) is observed at the beginning of each flip. AHMs have similarities to, but should not be confused with "chevron markings" that are found with brittle fractures. In contrast to AHMs, chevron markings point back to the origin. Notably, the frequency and direction (right rotation or left rotation) of the slant transitions is unique for each individual sample. In contrast, other features such as slant angle and slant height are identical. An overview of all obtained experimental fracture surfaces is given Figure 9.

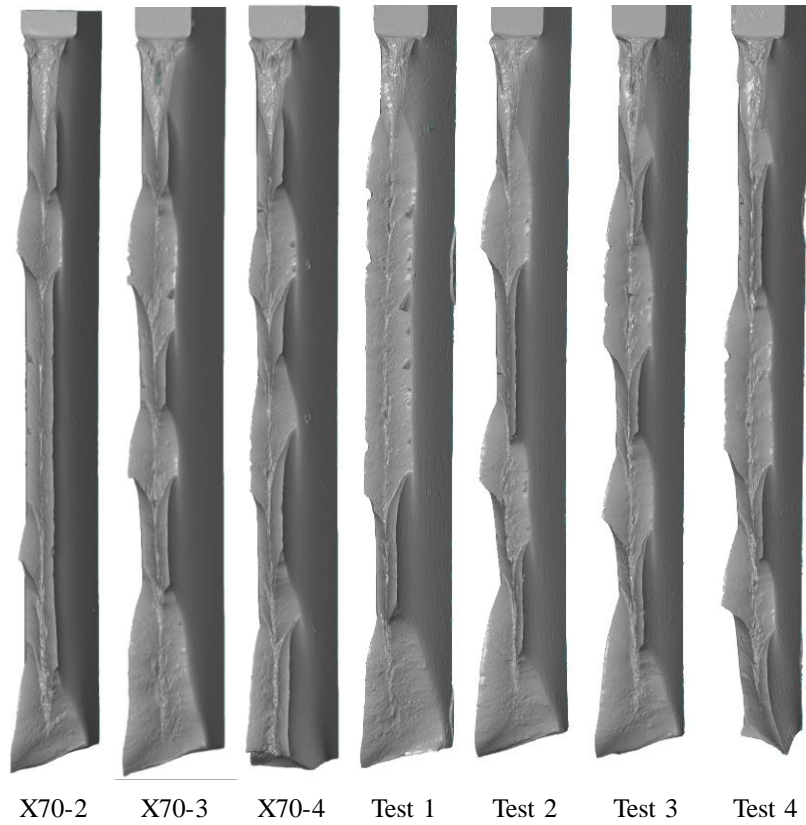


Figure 9: 3D scans of all obtained fracture surfaces (X70-2, X70-3, X70-4 obtained in [8]) show the variation of the alternating slant behaviour.

Using the scanned specimens, local plate thinning can be measured in the flat fracture zone and slant fracture zone. In Figure 10, it can be observed that a large amount of thinning is present at the flat surface whilst thinning in the slant fracture section is significantly lower which is consistent with the observations made by Hickey and Ravi-Chandar [26].

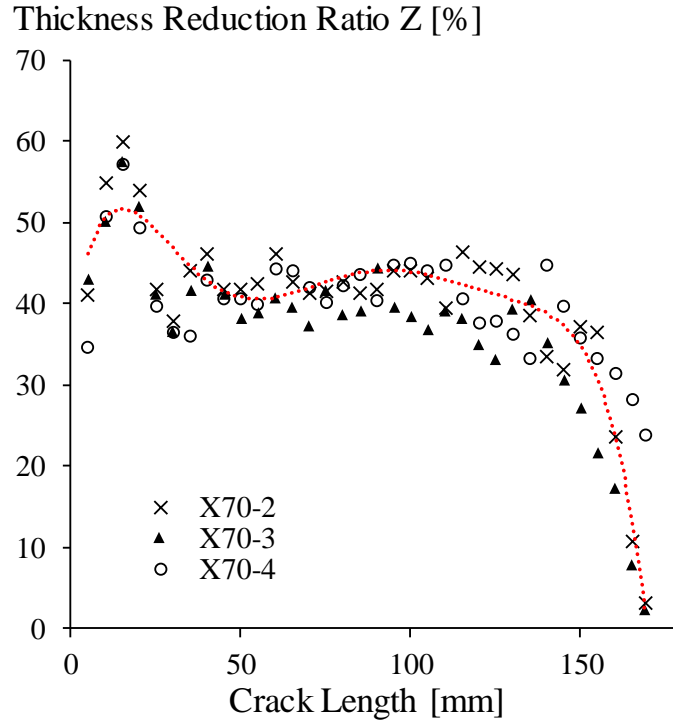


Figure 10: Thickness reduction ratio obtained using 3D GOM metrology software (data obtained in [8])

As a measure of resistance against ductile crack propagation, the energy release rate is determined based on energy values extracted from the load-displacement curve. The propagation energy is plotted as a function of crack length in Figure 11 (b). The crack length was measured optically on the surface of the specimen using the high-speed images. It should be noted that the actual crack extension at centre-thickness of the specimen is likely to extend further than the crack visible on the surface. Again, the three phases of failure can be distinguished. The energy release rate,  $R$ , is calculated for the second phase since that is the only region where dynamic crack propagation can be assumed. The  $R$ -values are determined in the same way as presented by Rivalin et al. [5]. Firstly, the load-displacement curve is integrated starting from the maximum load point, as shown in Figure 11 (a), divided by the original specimen thickness, and plotted as a function of the crack length. Finally, the  $R$ -values are defined as the slope of the constructed curve.

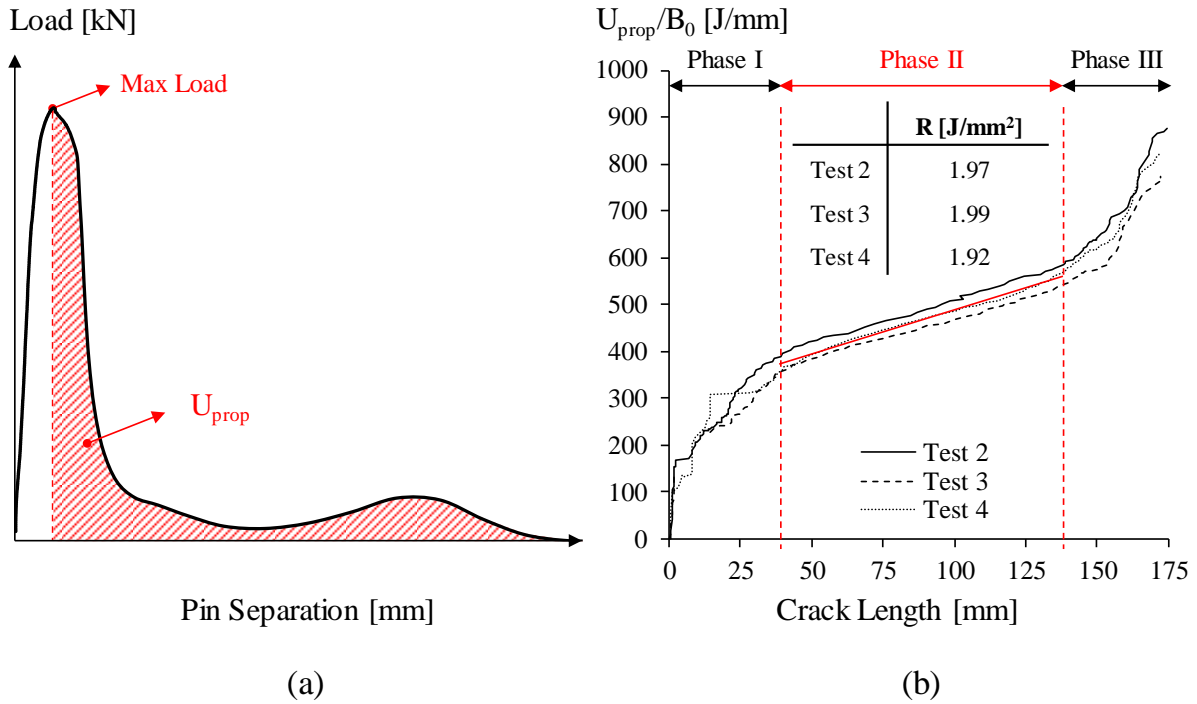


Figure 11: Evolution of the fracture energy indicates the three different phases of failure and subsequent values for the energy release rate.

#### 4.1.2 DIC Data Analysis

Further analysis of the fracture behaviour was performed using the image correlation procedure. Stereo DIC post-processing was performed on a selection of the obtained images to reduce computational effort. Image processing parameters were obtained through the performance analysis module implemented in the MatchID software. This procedure determined the optimal image processing parameters based on the resolution, FOV, and speckle size. Applying the parameters provided in Table 2 resulted in a good correlation throughout the majority of crack propagation. It should be noted that for the final tear-off phase, the specimen rotates out of the camera FOV which reduces the correlation quality. Figure 12 shows the strain distribution during dynamic crack propagation using stereo DIC.

Table 2: Overview of image processing parameters for Digital Image Correlation (DIC).

Parameter	
Stereo Angle $\phi$ ( $^{\circ}$ )	19.8
Grey Level Noise (%)	1.33
Subset Size (px)	15
Step Size (px)	7
In-plane Resolution ( $\mu\text{m}$ )	4.796

<b>Out-of-plane Resolution (<math>\mu\text{m}</math>)</b>	26.27
<b>VSG (px)</b>	29
<b>Strain Resolution (<math>\mu\text{m}/\text{mm}</math>)</b>	1.796

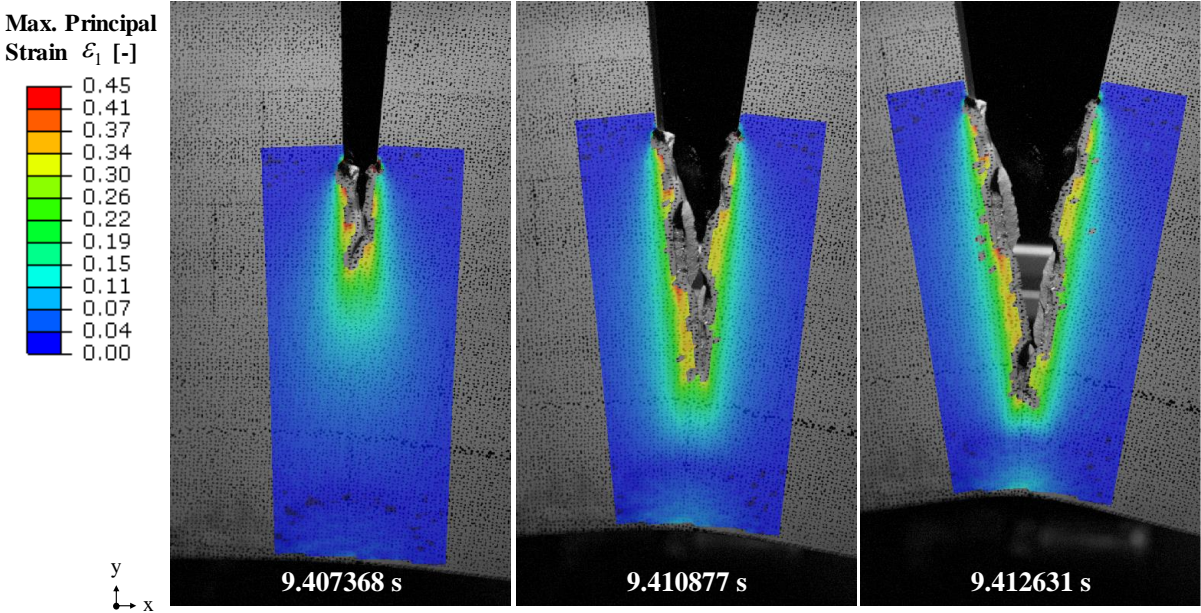


Figure 12: Strain correlation as crack progresses through the fracture specimen.

Out-of-plane movement was extracted on the left and right side with respect to the initial notch. A periodical out-of-plane behaviour could be determined and could be plotted in Figure 13 (a). The displacement on opposite sides of the notch is nearly identical, yet inverted in magnitude. This indicates the presence of a torsional component with the notch as rotational reference. Thus, the total displacement can be considered a measure of torsion present during the dynamic fracture phase. Figure 13 (b) shows that the total out-of-plane movement is similar in frequency and magnitude for each test however not identical.

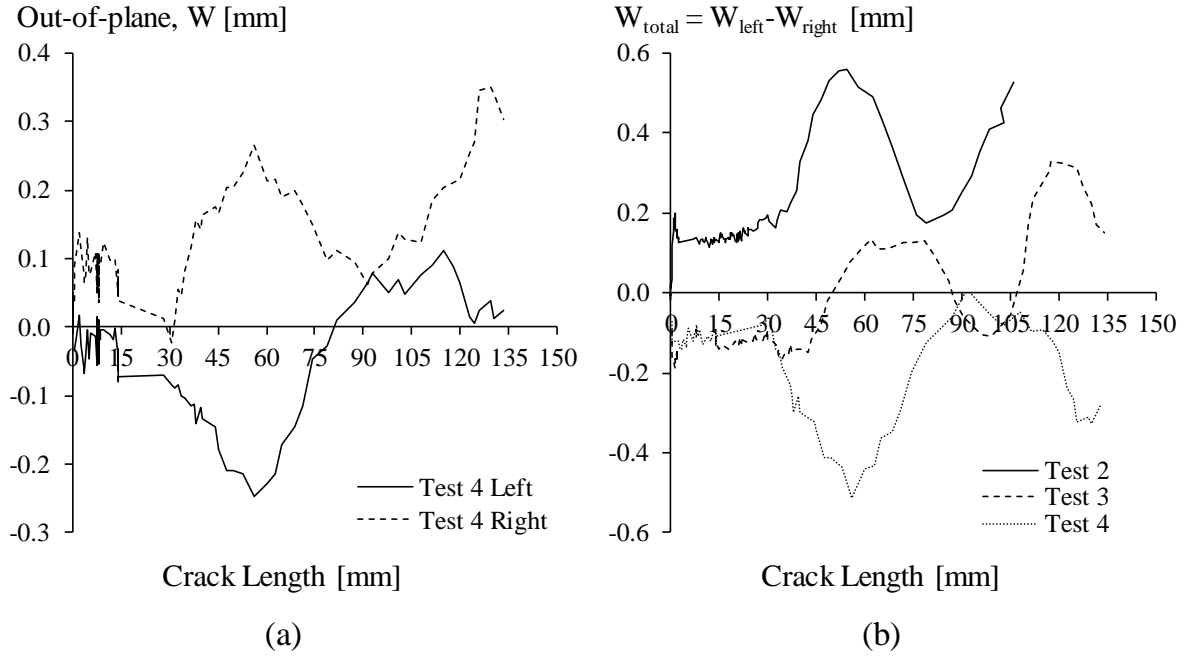


Figure 13: Extracted out-of-plane displacement extracted on left side and right side of the initial notch (a) and total out-of-plane deformation for all experiments (b).

The joints along the loading-axis of the DT3 system allows the specimen to adjust in order to avoid alignment errors. Consequently, the connector pin attached to steel bar that drives the disc springs, allows a rotation along the loading axis. Therefore, it can be assumed that the occurrence of this torsional movement is caused due to system parameters. However, during the dynamic phase, out-of-plane displacement are inevitable when shear fracture occurs. Even though this out-of-plane component is limited in magnitude, it is not possible to neglect its effects on the obtained results without further investigation. It should be noted that in reference model, created in previous investigation [8], an out-of-plane displacement could be observed. However, the order of magnitude is significantly smaller than observed during these experiments. Therefore, a torsional component similar to the experimental out-of-plane movement was implemented in the numerical model.

## 4.2 Numerical Results

### 4.2.1 MBW Data Correlation

Numerical data is extracted from both the reference model and the CTF model in order to provide a better insight regarding the influence of the CTF occurrence on the predictive performance of the model. Firstly, the load-displacement data shown in Figure 14 shows that the numerical models slightly underestimate the experimental peak load. Interestingly, both numerical curves are nearly identical. This suggests that the imposed out-of-plane displacement

does not influence the load-displacement behaviour. It is important to consider that energy-based fracture parameters such as initiation and fracture propagation energy are often extracted from the load-displacement curve. Producing an identical curve indicates that energy-based results are not affected by the implementation of an additional torsion load.

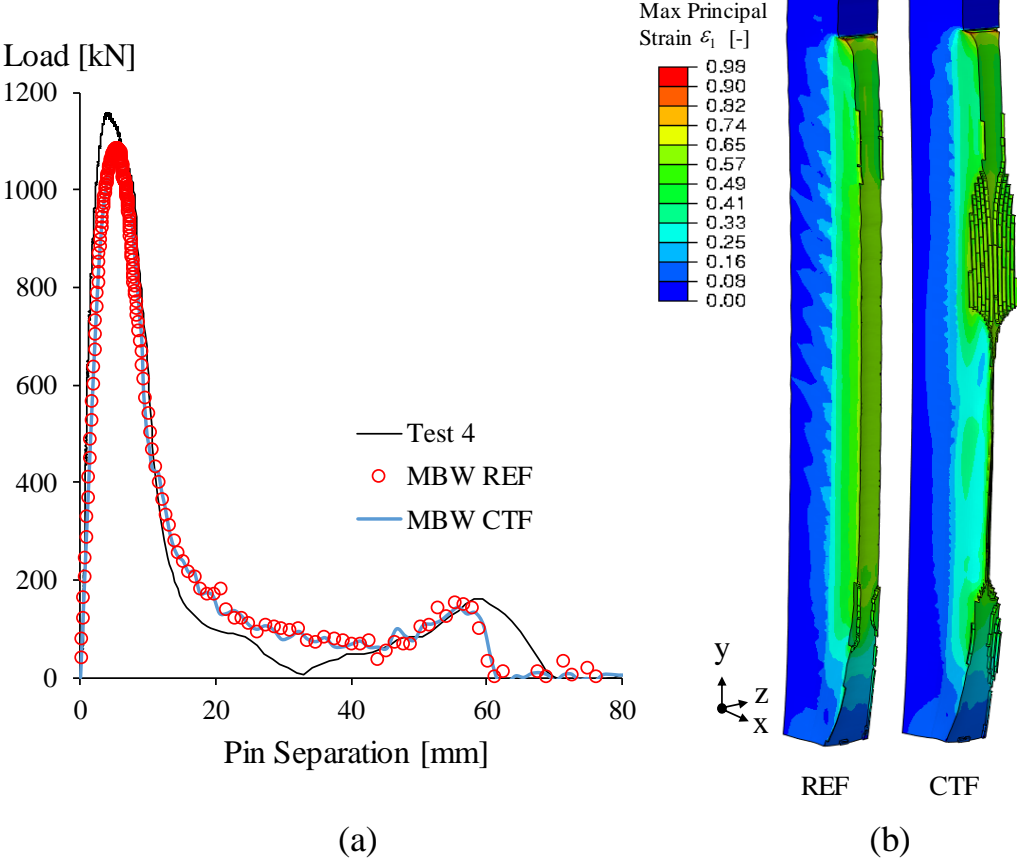


Figure 14: Validation of the experimental and numerical load-displacement data (a) and resulting fracture numerical fracture surfaces (b).

However, a clear distinction can be made between the resulting numerical fracture surfaces. In contrast to the reference model, the CTF model shows the same alternating slant behaviour as observed on the experimental fracture surfaces. As the resulting fracture surface is different, the crack progression is assessed in Figure 15.

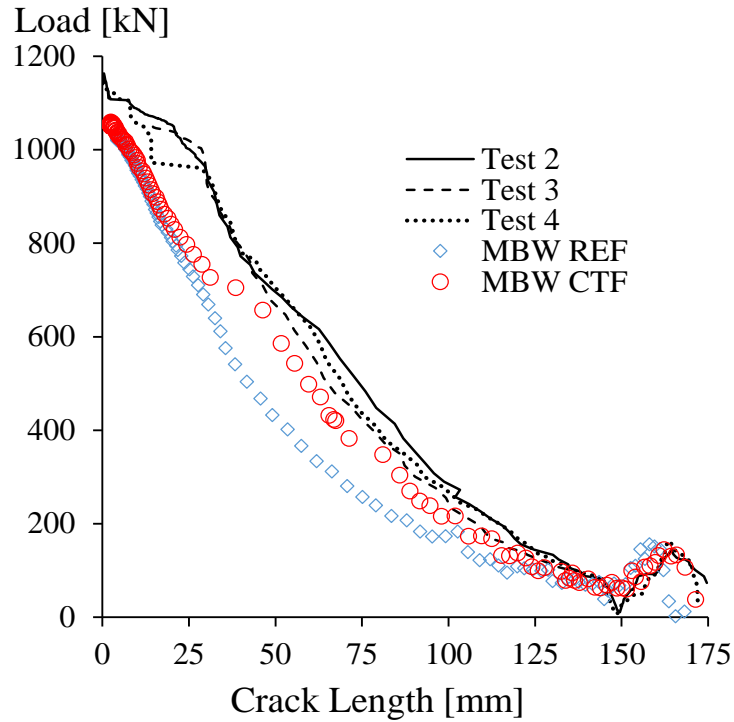


Figure 15: Validation of the load-drop as a function of the crack extensions.

The CTF model shows a slight improvement in correlation between numerical and experimental load drop during crack propagation. It should be noted that this does not necessarily indicate a difference in fracture behaviour. To ensure consistency with experimental data, the crack extension is measured at the specimen surface. Consequently, it can only be concluded that the visible crack length during slanted propagation deviates from the symmetrical crack propagation of the reference model. Furthermore, the visible fracture path of the CTF model is consistent with the path observed in the high-speed images as it shows the same wave-like behaviour during dynamic propagation. A qualitative comparison between the experimental fracture path and respective strain distribution is shown in Figure 16. Here, LE11 is defined as the logarithmic strain component along the x-axis.

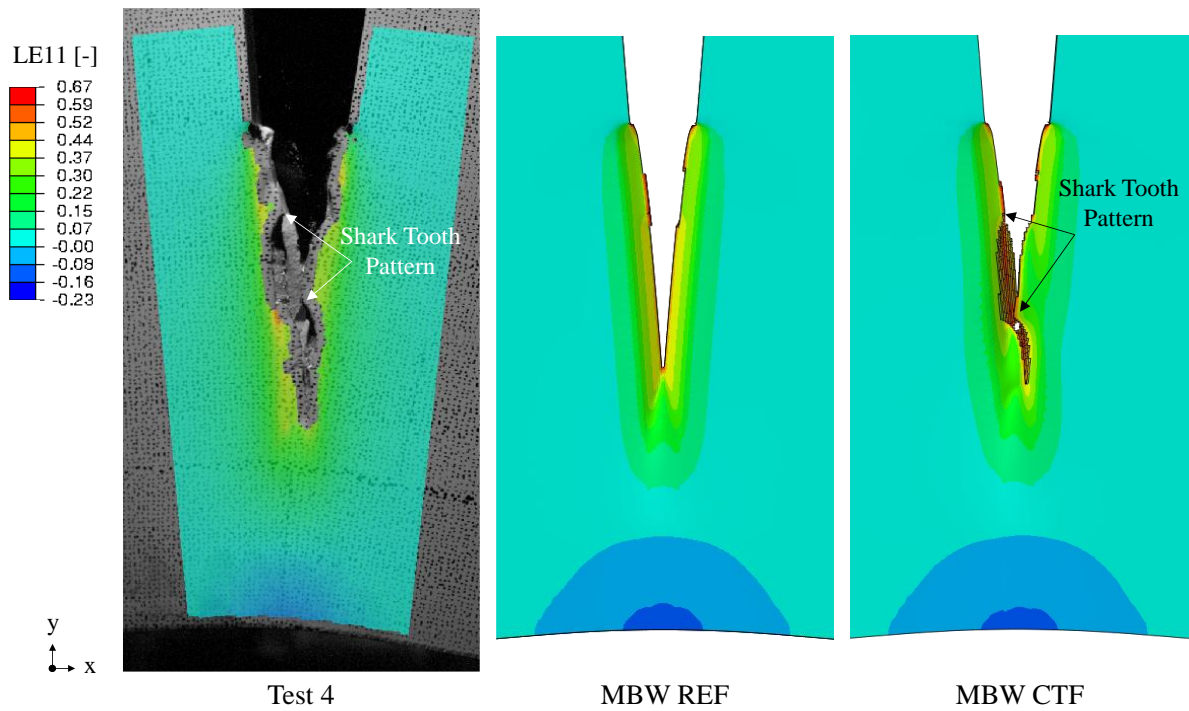


Figure 16: Qualitative comparison between experimental DIC fracture path and strain distribution with the numerical CTF model.

Full field strain distribution shows a good correlation during fracture propagation. Currently, it is challenging to achieve image correlation close to the edges of the fracture path. Consequently, the strain concentrations close to the fracture path do not show satisfactory correlation. On the other hand, the compressive strain concentration during specimen rotation is clearly visible. Furthermore, the same typical crack progression can be observed leaving a shark tooth pattern on the specimen surface. Using a point extraction, the exact strain value as a function of the crack length could be plotted. The graph in Figure 17 shows a good correlation between experimental DIC correlation and both numerical models.

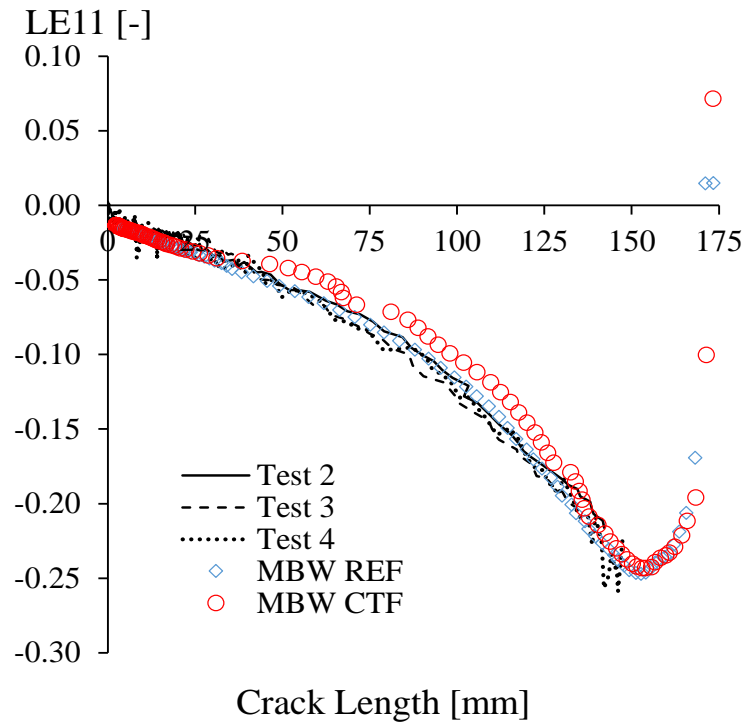


Figure 17: Correlation between experimental and numerical compressive strain in the final tear-off zone.

Regarding the fracture surface, it could be observed that AHM formation is also present on the numerical fracture surface as shown in Figure 18. The same sequence of AHM formation, CTF transition, and AHM formation is visible. This supports the hypothesis that both mechanism of AHM and CTF are related. The formation of AHMs has been attributed to the presence of microstructural banding which is a form of delamination [27]. Tanaka et al. [28] have identified a strong influence of strain hardening on the occurrence of delamination. Regarding the CTF mechanism, Felter and Nielsen [14] also indicated strain hardening capacity as one of the critical material parameters. Therefore, strain hardening can be identified as a governing factor as it is the common parameter causing the formation of material-dependent phenomena of CTF and AHM formation. However, the data from this study suggest that the out-of-plane displacement might be the main catalyst to introduce the CTF mechanism.

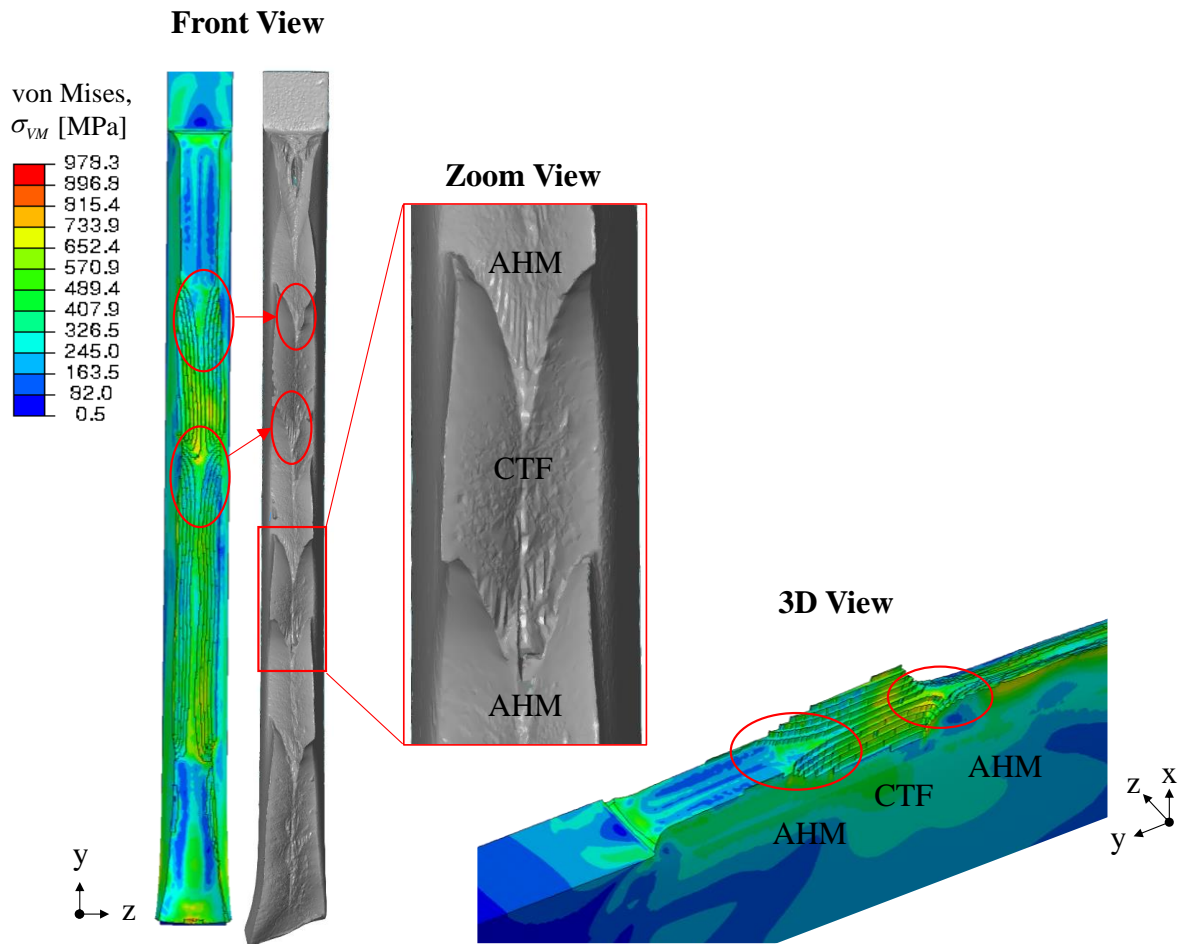


Figure 18: Formation of AHM and CTF on the numerical fracture surface and scanned experimental fracture surface.

Moreover, the recent research project SARCO2 allows to make a clear link between AHM formation and the loading conditions during pipeline failure. This project conducted two full-scale burst tests using CO<sub>2</sub>. One of the two pipes, constructed from API X65 grade, showed the formation of AHMs, as shown in Figure 19, after failure in a fully ductile manner.

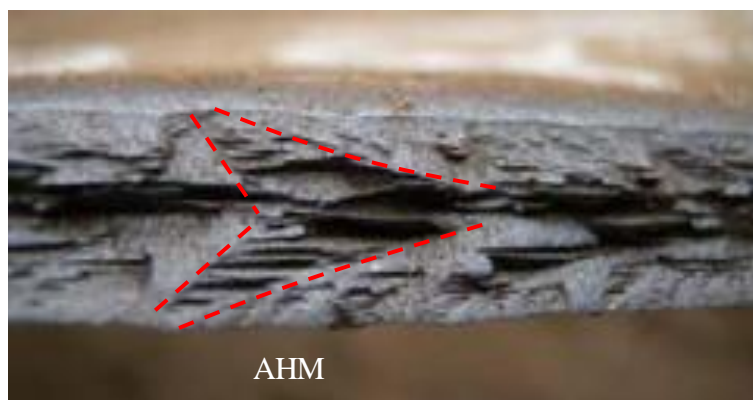


Figure 19: Fracture surface of the first full-scale burst test during SARCO2B project shows the formation of AHMs [29].

## 4.2.2 CTF Mechanism Analysis

The mechanism of CTF was investigated by analysing the stress state during dynamic crack propagation. Figure 20 shows stress triaxiality and Lode angle parameters as indicators for the present stress state. At the moment a CTF transition occurs, a neutral Lode angle zone is formed in front of the crack tip whilst a positive triaxiality is formed. It is clear that the crack path deviates in the direction of the formed zones. Extracting values for the neutral Lode angle parameter and a triaxiality of approximately 0.67 indicates a plane strain tension stress state at the moment of crack path deviation. Notably, the triaxiality value continues to increase up to a value of 1, which indicates a progressive shift towards a generalised plain strain or generalised shear stress state.

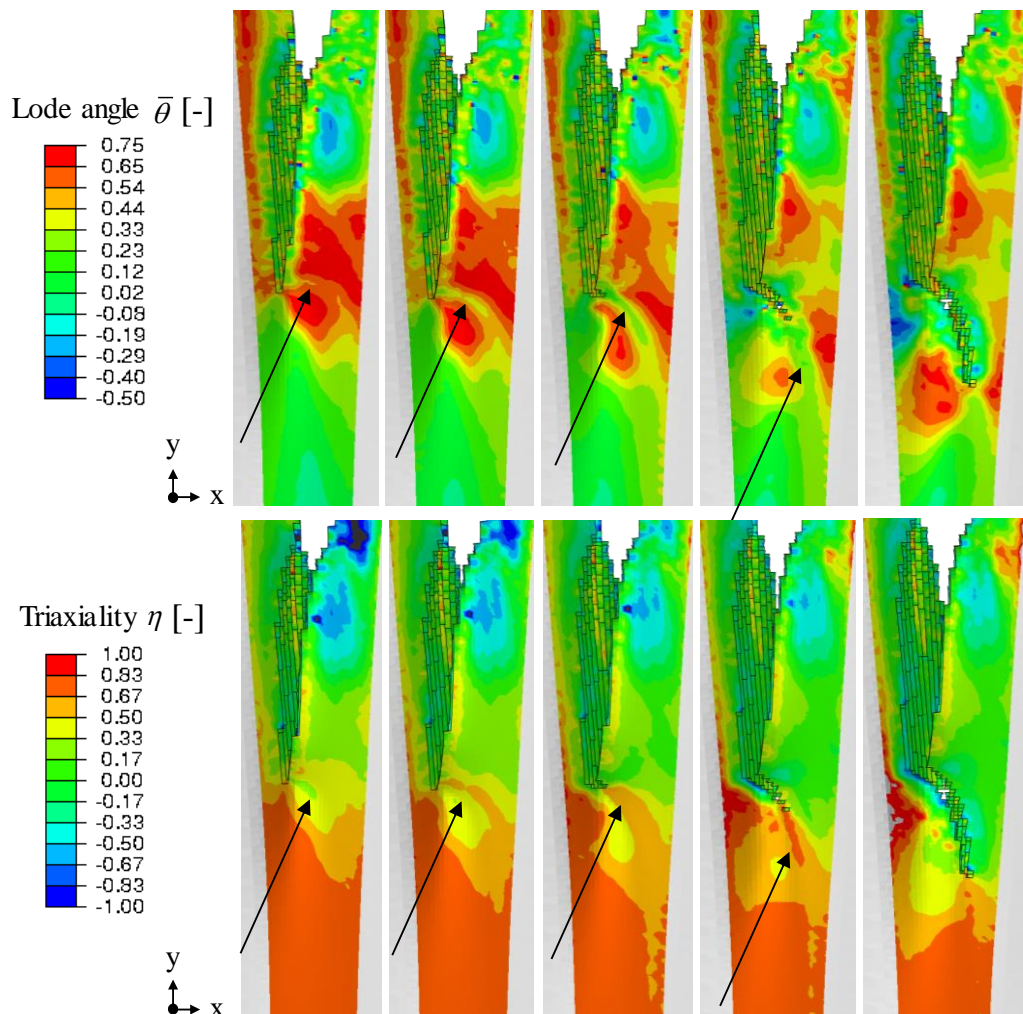


Figure 20: Stress state variation during CTF transition in terms of the Lode angle parameter (top) and the stress triaxiality (bottom).

Now, if the stress state is changed due to the out-of-plane oscillation, this should be observed at the crack front as well. Figure 21 shows the Lode angle parameter contours plotted on the

cross sectional view of the crack front. As the crack progresses, the Lode angle parameter remains neutral. Notably, the crack front changes shape as the crack progresses.

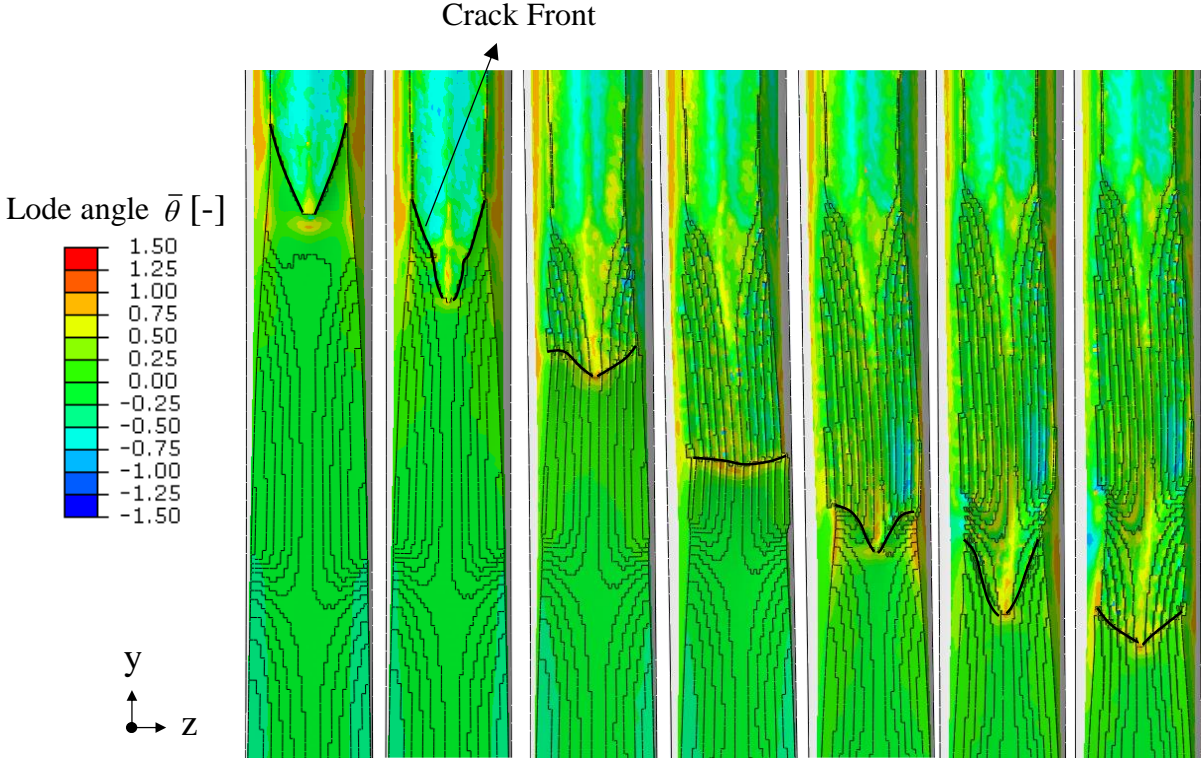


Figure 21: Perpendicular view on the crack front showing that the Lode angle parameter remains neutral as the crack progresses through the fracture ligament.

Figure 22 shows that the stress triaxiality, in contrast to the Lode angle, changes together with the shape of the crack front. A high stress triaxiality concentration is present at the crack tip, which indicates lower ductility at the centre of the specimen. As the out-of-plane oscillation increases in amplitude, observed crack tunnelling associated with plane strain tension transforms into a straight line typical for shear failure. Together with the crack front, the stress triaxiality concentration relocates along the width of the new crack front. This indicates a shift in stress state at the crack tip from plane strain tension to a generalised shear. During the shape transition of the crack front, an AHM is formed. From Figure 22, it is clear that this process is repeated as the crack progresses. In comparison, the reference model shows symmetrical crack tunnelling as observed in [8], which clarifies the difference in the obtained numerical fracture surfaces.

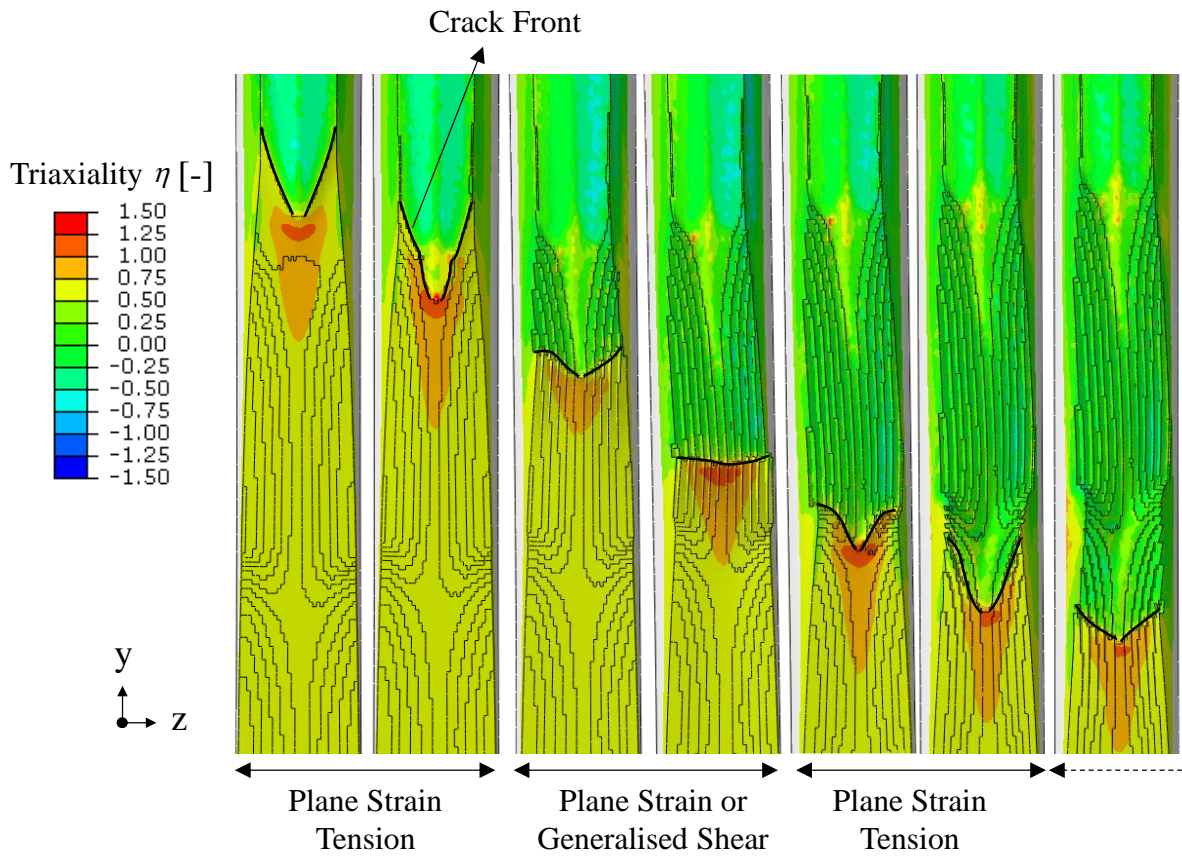


Figure 22: Perpendicular view on the crack front indicating the shape change of the crack front under influence of the out-of-plane oscillation.

This repeated process suggests that the stress state at the crack tip changes together with the changing amplitude of the oscillation. Therefore, the stress tensor at different point along the crack front were extracted to assess the direct effect on the stress balance. A significant change was found with respect to the shear component  $S_{xz}$  along the crack front. Figure 23 indicates that the through-thickness shear stress component  $S_{xz}$ , initially shows an equilibrium with a resultant of zero along the crack front. When the out-of-plane displacement occurs, the balance is removed and the  $S_{xz}$  shear component aligns across the crack front creating a non-zero resultant shear component.

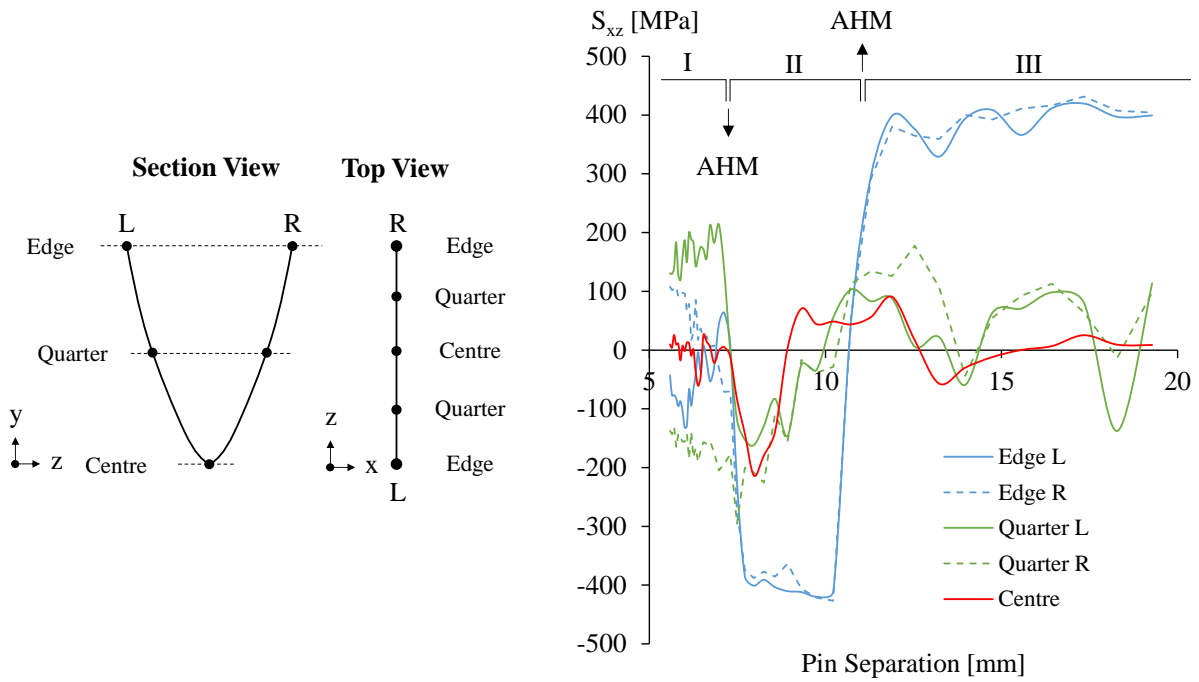


Figure 23: Shear stress component  $S_{xz}$  shows the same oscillation behaviour as the applied out-of-plane vibration.

In Figure 23, stage I refers to the reference behaviour as the out-of-plane displacement is not yet applied. Stage II and stage III show the behaviour of the  $S_{xz}$  shear component as the amplitude of the vibration changes. An AHM is formed during the transition from one stage to the other. The influence on the resulting maximum principal stress tensor is visualised in Figure 24 for each respective stage. In this symbol plot, the elements at the crack tip are isolated and the maximum principal stresses are indicated by red arrows. It can be seen that the maximum principal stress tensor rotates towards the plane of maximum shear. Coincidentally, the crack front rotates towards the  $-45^\circ$  plane or  $+45^\circ$  with respect to the sign of the shear stress component and subsequent angle of the maximum principal stress tensor.

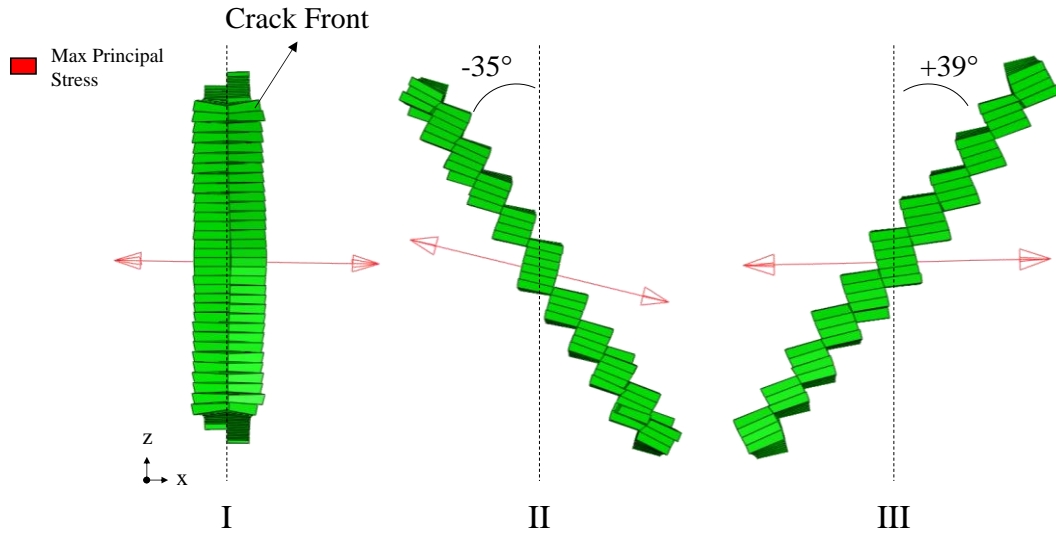


Figure 24: Resultant maximum principal stress tensor rotates as the shear component varies under the influence of the out-of-plane vibration.

The angle under which the maximum principal stress acts,  $\theta_p$ , can be determined through derivation of the stress transformation equation. The resulting equation to calculate  $\theta_p$  can be formulated as:

$$\tan 2\theta_p = \frac{2S_{xz}}{S_x - S_z}$$

with  $S_{xz}$  the shear component along the xy-plane,  $S_x$  and  $S_z$  the normal stress components along the x-axis and z-axis respectively. The angle of maximum principal stress along the crack front can thus be plotted as shown in Figure 25 (a). At the crack front edge, angle values up to  $36^\circ$  are reached which are similar to the rotation of the crack front and the angle of the slanted fracture surface. This variation of  $\theta_p$  indicates a direct link to the rotated fracture surface. It is important to note that even though the stress balance is shifted, the effective stress along the crack front, shown in Figure 25 (b) remains constant.

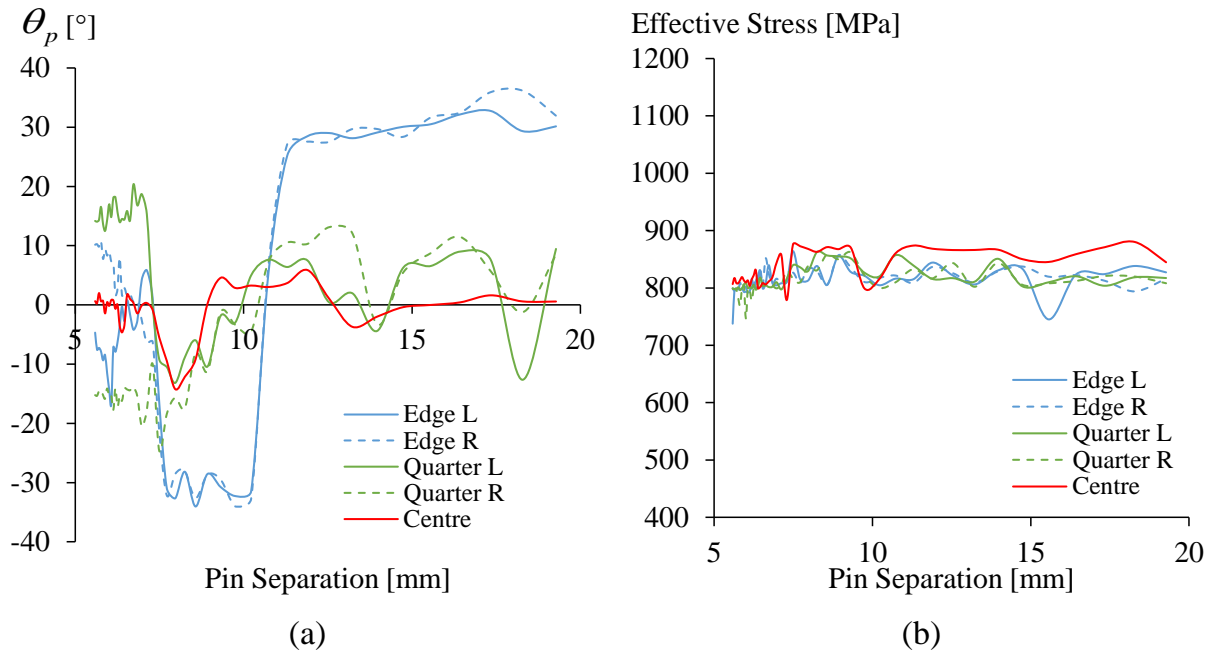


Figure 25: The angle of maximum principal stress with respect to the original loading direction varies (a) whilst the effective stress remains quasi-constant (b).

The rotation maximum principal stress rotates according to the out-of-plane oscillation indicates the reason of stress state rotation. As the effect of stress state on the plastic deformation and damage behaviour are considered in the MBW, the material response will be affected. This is demonstrated in Figure 26 where equivalent plastic strain, stress triaxiality, and maximum principal stress along the crack front are plotted. It should be noted that as plastic strain concentration rotates, damage variable  $D$  follows the same behaviour. Furthermore, in the MBW model, a plane strain stress state with increasing stress triaxiality will provide the lowest value for damage initiation strain (Equation 7). In addition, the lowest possible value for the critical damage parameter is returned (Equation 9). Consequently, in the MBW model considers a plane strain state with increasing stress triaxiality as increasingly critical condition. This is also apparent in the formulated MBW fracture locus [24]. As the crack front will follow the most critical path, a slanted fracture surface is generated. However, as shown in Figure 25 (b), the effective stress remains constant which explains why the material response in terms of reaction force, does not change with rotation of the crack front.

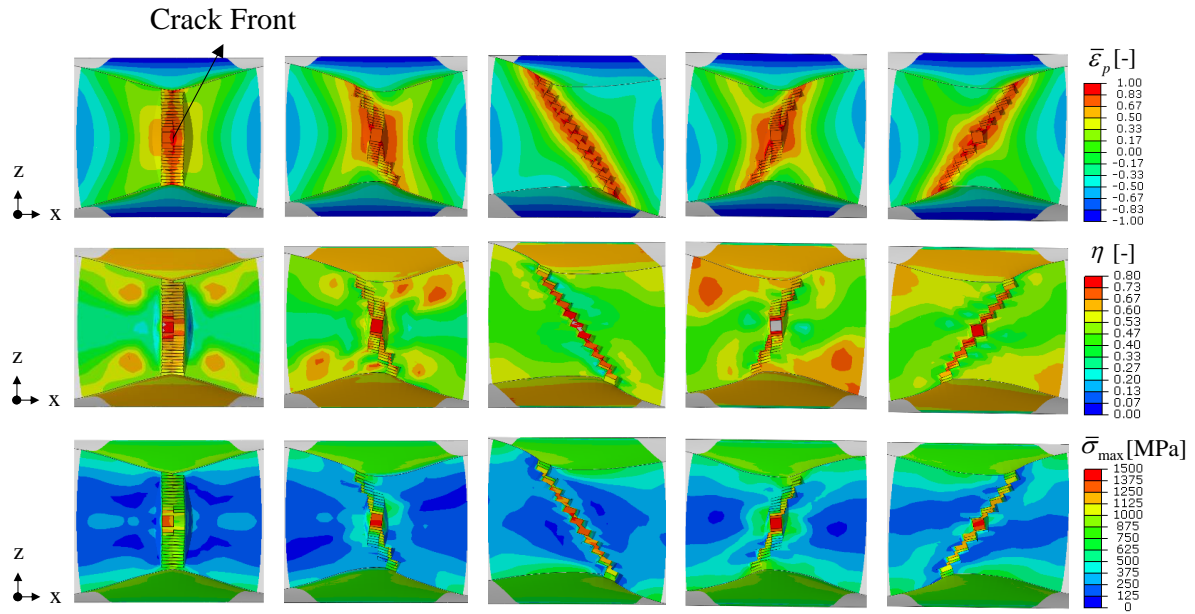


Figure 26: Rotation of the plastic strain, stress triaxiality, and principal stress concentrations as result of the out-of-plane vibration.

In summary, the presence of an out-of-plane vibration introduces a shift in the stress balance. The through-thickness shear component  $S_{xz}$  changes together with the amplitude of the oscillation. As a consequence, the direction of the maximum principal stress tensor shifts towards a  $45^\circ$  angle with respect to the original loading direction. Subsequently, material deformation and damage accumulation occur according to the stress tensor rotation. This results in the slanted fracture surface as the crack front represents the most critical path for crack propagation. The AHM formation occurs when the orientation of the resultant stress tensor passes the original alignment with the loading line along the x-axis.

The CTF phenomenon is observed in both aluminium alloys and high grade steels, it is observed under quasi-static and dynamic conditions, and it occurs primarily in plane strain experiments. This formulation of the stress state as governing factor for the CTF occurrence remains valid when applied to these observations made in literature. In terms of pipeline failure, this suggests that CTF features on the fracture surface indicate the presence of an out-of-plane loading which could result from soil backfill, bending moment, etc. This suggests that CTF could provide a better understanding of the conditions present at the moment of failure or potentially indicate the cause of failure. However, there is currently insufficient in-field data available to conclude that CTF can indicate the cause of failure.

## 5 Conclusions

The occurrence of CTF has been investigated using the experimental DT3 setup in combination with a high-speed stereo DIC setup. To assist the experimental testing, numerical models were created using the MBW material model to describe plasticity and damage behaviour. The mechanisms underlying CTF were identified, and the impact on the results was thoroughly examined. Based on this comprehensive investigation, the following conclusions have been formulated:

- An out-of-plane vibration was identified during the dynamic crack propagation, which introduced an additional torsional loading component. The implementation of an out-of-plane displacement into the numerical model provokes the occurrence of CTF and formation of AHMs.
- The numerical model produced a nearly identical wave-like fracture path as observed on the high-speed images as well as a similar fracture surface characterised by alternating slant typical for the CTF phenomenon.
- The out-of-plane oscillation influences the stress balance and results in a rotation of the maximum principal stress tensor towards the plane of maximum shear. This rotation is controlled by the through-thickness shear component. Consequently, the stress state at the crack front is altered which causes the formation of the slanted fracture surface.
- The load-displacement curve is not affected by the implementation of an additional torsional load, as the value of the effective stress remains constant. This implies that, interestingly, the CTF phenomenon does not influence the fracture resistance as fracture resistance parameters are often based on energy values extracted from the load-displacement curve.
- This study suggests that the CTF phenomenon could provide valuable insight in the conditions under which a pipeline failure occurred and subsequently could potentially indicate a cause of failure. However, additional studies and investigation on burst-tested pipes and in-field failures are required to conclude whether there is a direct link between the CTF phenomenon and the conditions at the moment of failure.

## 6 Acknowledgements

The authors gratefully acknowledge the support of the Research Foundation Flanders (FWO) via PhD fellowship grant 1SB6420N. The technical support and contribution of Koen Bracke

and OCAS ArcelorMittal Global R&D Gent are also acknowledged. The authors also acknowledge Dr. Pascal Lava for the use of the MatchID software.

## 7 References

- [1] F. Van den Abeele and B. Paermentier, “Fracture Propagation Control for CO2 Pipelines: State-Of-The-Art and Challenges,” in *Technology for Future and Ageing Pipelines*, Gent, 2022.
- [2] G. Mannucci, G. Demofonti and M. Di Biagio, “X100 - Fracture initiation and propagation,” ECSC Report, 2005.
- [3] G. Wilkowski, W. Maxey and R. Eiber, “Problems in Using the Charpy & Drop Weight Tear Test for High Toughness Q&T Steels,” in *What Does Charpy Energy Really Tell us?*, ASM, 1978, pp. 201-226.
- [4] Y. Hioe, G. Wilkowski, M. Fishman and M. Myers, “Determination of Brittle-to-Ductile Transition Temperatures of Large-Diameter TMCP Linepipe Steel with High Charpy Energy by Use of Modified West Jefferson Testing,” in *Proceedings of the 11th International Pipeline Conference*, Calgary, Alberta, Canada, 2016.
- [5] F. Rivalin, A. Pineau, M. Di Fant and J. Besson, “Ductile tearing of pipeline-steel wide plates I. Dynamic and quasi-static experiments,” *Engineering Fracture Mechanics*, no. 68, pp. 329-345, 2001.
- [6] F. Rivalin, J. Besson, A. Pineau and M. Di Fant, “Ductile tearing of pipeline-steel wide plates II. Modeling of in-plane crack propagation,” *Engineering Fracture Mechanics*, no. 68, pp. 347-364, 2001.
- [7] T. T. Luu, *Déchirure ductile des aciers à haute résistance pour gazoducs (X100)*, Paris: École Nationale Supérieure des Mines de Paris, 2007.
- [8] B. Paermentier, S. Cooreman, P. Verleysen, S. Chandran, S. Coppieters and R. Talemi, “A Dynamic Tensile Tear Test Methodology to Characterise Dynamic Fracture Behaviour of Modern High-Grade Pipeline Steels,” *Engineering Fracture Mechanics*, vol. 272, 2022.

- [9] T. Tagawa, S. Igi, S. Kawaguchi, M. Ohata and F. Minami, “Fractography of burst-tested linepipe,” *International Journal of Pressure Vessels and Piping*, vol. 89, pp. 33-41, 2012.
- [10] L. dos Santos Pereira, R. Figueiredo Moco and G. Henrique Bolognesi Donato, “Ductile fracture of advanced pipeline steels: study of stress states and energies in dynamic impact specimens - CVN and DWTT,” in *ECF22 - Loading and Environmental effects on Structural Integrity*, Belgrade (Serbia), 2018.
- [11] J. Chattopadhyay, B. K. Dutta and H. S. Kushwaha, “Experimental and analytical study of three point bend specimen and throughwall circumferentially cracked straight pipe,” *International Journal of Pressure Vessels and Piping*, vol. 77, pp. 455-471, 2000.
- [12] B. C. Simonsen and R. Törnqvist, “Experimental and numerical modelling of ductile crack propagation in large-scale shell structures,” *Marine Structures*, vol. 17, pp. 1-27, 2004.
- [13] C. L. Felter and K. L. Nielsen, “Assisted crack tip flipping under Mode I thin sheet tearing,” *European Journal of Mechanics - A/Solids*, vol. 64, pp. 58-68, 2017.
- [14] K. L. Nielsen and C. L. Felter, “Parameter window for assisted crack tip flipping: Studied by a shear extended Gurson model,” *International Journal of Solids and Structures*, vol. 171, no. 15, pp. 135-145, 2019.
- [15] K. L. Nielsen and C. Gundlach, “Crack tip flipping under mode I tearing: Investigated by X-ray tomography,” *International Journal of Solids and Structures*, vol. 118, pp. 119-127, 2017.
- [16] Haihao Piping, “What is Hydrogen-Induced Cracking (HIC),” [Online]. Available: <https://www.haihaopiping.com/what-is-hydrogen-induced-cracking-hic.html>.
- [17] US Department of Transportation, “Failure Investigation Report: Material Failure – Mechanical Damage from Original Construction - TC Oil Pipeline Operations, Inc.,” Office of Pipeline Safety’s Accident Investigation Division, USA, 2018.
- [18] US Department of Transportation, “Pipeline Safety: Pipeline Damage Prevention Programs,” United States Government Printing Office, USA, 2015.

- [19] MatchID, *MatchID 2022*, 2022.
- [20] R. Talemi, S. Cooreman and D. Van Hoecke, “Finite element simulation of dynamic brittle fracture in pipeline steel: A XFEM-based cohesive zone approach,” *Journal of Materials: Design and Applications*, vol. 5, no. 232, pp. 357-370, 2018.
- [21] D. Novokshanov, M. Sharaf, S. Münstermann and J. Lian, “A new model for upper shelf impact toughness assessment with a computationally efficient parameter identification algorithm,” *Engineering Fracture Mechanics*, vol. 148, pp. 281-303, 2015.
- [22] Dassault Systèmes, *ABAQUS Documentation 2019*, Providence, United States, 2019.
- [23] J. Lian, M. Sharaf, F. Archie and S. Münstermann, “A hybrid approach for modelling of plasticity and failure behaviour of advanced high-strength steel sheets,” *International Journal of Damage Mechanics*, vol. 22, no. 2, pp. 188-218, 2013.
- [24] Y. Bai and T. Wierzbicki, “A new model of metal plasticity and fracture with pressure and Lode dependence,” *International Journal of Plasticity*, vol. 24, no. 6, pp. 1071-1096, 2008.
- [25] B. Wu, X. Li, Y. Di, V. Brinnel, J. Lian and S. Münstermann, “Extension of the modified Bai-Wierzbicki model for predicting ductile fracture under complex loading conditions,” *Fatigue & Fracture of Engineering Materials & Structures*, vol. 40, no. 12, pp. 2152-2168, 2017.
- [26] W. Hickey and K. Ravi-Chandar, “Transition from Flat to Slant Fracture in Ductile Materials,” *Recent Trends in Fracture and Damage Mechanics*, pp. 215-235, 2016.
- [27] R. Schofield, G. Rowntree, N. V. Sarma and R. T. Weiner, “‘Arrowhead’ fractures in controlled-rolled pipeline steels,” *Metals Technology*, pp. 325-331, 1974.
- [28] M. Tanaka, T. Manabe, T. Morikawa and K. Higashida, “Mechanism Behind the Onset of Delamination in Wire-drawn Pearlitic Steels,” *Iron and Steel Institute of Japan (ISIJ) International*, vol. 60, no. 11, pp. 2596-2603, 2020.
- [29] M. Di Biagio, M. Erdelen-Peppler, S. Jäger, C. Kalwa, C. Kassel, H. Brauer, W. Wessel, N. Voudouris, C. M. Spinelli, S. Saysset and R. Cooper, “Requirements for safe and

reliable CO2 transportation pipeline (SARCO2),” European Commission, Brussels, 2017.